CMS Physics Analysis Summary

Contact: cms-pag-conveners-susy@cern.ch 2013/05/16

Search for top-squark pair production in the single lepton final state in pp collisions at $\sqrt{s} = 8$ TeV

The CMS Collaboration

Abstract

This report presents a search for the pair production of top squarks in events with a single isolated electron or muon, jets, large missing transverse energy, and large transverse mass. The data sample corresponds to an integrated luminosity of 19.5 fb^{-1} of pp collisions collected in 2012 by the CMS experiment at the LHC, at a center-of-mass energy $\sqrt{s} = 8$ TeV. No significant excess in data is observed above the expected standard model backgrounds. The results are interpreted in the context of supersymmetric models with pair production of top squarks that decay either to a top quark and a neutralino or to a bottom quark and a chargino. Depending on the decay, the results probe top squarks with masses up to about 650 GeV.

1 Introduction

The standard model (SM) has been extremely successful at describing particle physics phenomena. However, it suffers from such shortcomings as the hierarchy problem, where fine-tuned cancellations of large quantum corrections are required in order for the Higgs boson to have a mass at the electroweak symmetry breaking scale of order 100 GeV [1–6]. Supersymmetry (SUSY) is a popular extension of the SM that postulates the existence of a superpartner for every SM particle, with the same quantum numbers but differing by one half unit of spin. SUSY provides a natural solution to the hierarchy problem through the cancellations of the quadratic divergences of the top quark and scalar top squark loops. In addition, it provides a connection to the cosmological sector, with the lightest supersymmetric particle (LSP), if neutral and stable, serving as a dark matter candidate.

This note describes a search for the pair production of top squarks using the full dataset collected at $\sqrt{s} = 8$ TeV by the Compact Muon Solenoid (CMS) experiment [7] at the Large Hadron Collider (LHC) during 2012, corresponding to an integrated luminosity of 19.5 fb^{-1}. The results presented here constitute an extension of a previous CMS search [8]. This search is motivated by the observation that relatively light top squarks, with masses less than several hundred GeV, are necessary if SUSY is to be the "natural", i.e., not fine-tuned, solution to the gauge hierarchy problem [9–13]. These constraints are especially relevant given the recent discovery of a particle that closely resembles the Higgs boson, with a mass of $\sim$125 GeV [14–16]. Searches for top-squark pair production have also been performed by the ATLAS collaboration at the LHC in several final states [17–21], and by the CDF [22] and D0 [23] collaborations at the Tevatron.

The search presented here focuses on two decay modes of the top squark ($\tilde{\mathrm{t}}$): $\tilde{\mathrm{t}} \to \mathrm{t}\tilde{\chi}_1^0$ and $\tilde{\mathrm{t}} \to \mathrm{b}\tilde{\chi}_1^+$. These modes are expected to have large branching fractions if kinematically accessible. Here the neutralinos ($\tilde{\chi}^0$) and charginos ($\tilde{\chi}^\pm$) are the mass eigenstates formed by the linear combination of the gauginos and higgsinos, fermionic superpartners of the gauge and Higgs bosons, respectively. The charginos are unstable and subsequently decay into neutralinos and W bosons, leading to the following processes of interest: $\mathrm{pp} \to \tilde{\mathrm{t}}\bar{\tilde{\mathrm{t}}}^* \to \mathrm{t}\bar{\mathrm{t}}\tilde{\chi}_1^0\tilde{\chi}_1^0 \to \mathrm{b}\bar{\mathrm{b}}\mathrm{W}^+\mathrm{W}^-\tilde{\chi}_1^0\tilde{\chi}_1^0$ and $\mathrm{pp} \to \tilde{\mathrm{t}}\bar{\tilde{\mathrm{t}}}^* \to \mathrm{b}\bar{\mathrm{b}}\tilde{\chi}_1^+\tilde{\chi}_1^- \to \mathrm{b}\bar{\mathrm{b}}\mathrm{W}^+\mathrm{W}^-\tilde{\chi}_1^0\tilde{\chi}_1^0$, as displayed in Fig. 1. The lightest neutralino $\tilde{\chi}_1^0$ is considered to be the stable LSP, which escapes without detection and results in large missing transverse energy ($E_\mathrm{T}^\mathrm{miss}$).

The signatures in the $\tilde{\mathrm{t}} \to \mathrm{t}\tilde{\chi}_1^0$ and $\tilde{\mathrm{t}} \to \mathrm{b}\tilde{\chi}_1^+$ decay modes include four high transverse momentum (p_T) jets, two of which are from bottom quarks, and $E_\mathrm{T}^\mathrm{miss}$. The requirement of exactly one isolated, high p_T electron or muon serves to suppress many of the backgrounds present in

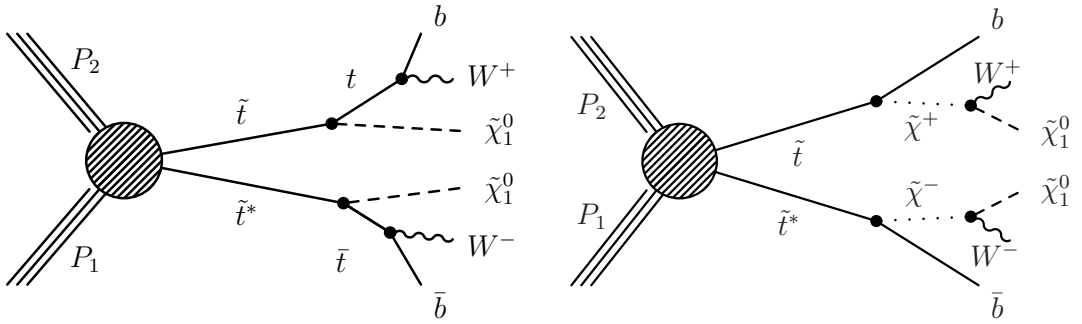

Figure 1: Diagram for top-squark pair production for the $\tilde{\mathrm{t}} \to \mathrm{t}\tilde{\chi}_1^0 \to \mathrm{bW}\tilde{\chi}_1^0$ decay mode (left) and the $\tilde{\mathrm{t}} \to \mathrm{b}\tilde{\chi}_1^+ \to \mathrm{bW}\tilde{\chi}_1^0$ decay mode (right).

the all-hadronic channel, while retaining high signal efficiency due to the presence of two W bosons in the final state. For the $\tilde{t} \to t\tilde{\chi}_1^0$ model only, three of the jets originate from the decay of a top quark, a propery that is exploited in the search.

The largest backgrounds in this search are from semi-leptonic decays of $t\bar{t}$ and W+jets events. These backgrounds contain a single leptonically decaying W boson; the transverse mass, defined as $M_T \equiv \sqrt{2E_T^{miss} p_T^{\ell}(1-\cos(\Delta\phi))}$, where p_T^{ℓ} is the transverse momentum of the lepton and $\Delta\phi$ is the difference in azimuthal angles between the lepton and E_T^{miss}, has a kinematic endpoint $M_T < M_W$. For signal, the presence of LSPs in the final state allows M_T to exceed M_W. Hence we search for an excess of events with large M_T. The dominant background with large M_T is dilepton $t\bar{t}$ where one of the leptons is not identified, since the presence of the additional neutrino from the second leptonically decaying W boson leads to large E_T^{miss} and M_T. Compared to the result described in [8], this analysis uses additional kinematic discriminants, along with an improved veto on additional leptons. The primary results of our search use boosted decision tree (BDT) techniques, and we also pursue a cut-based analysis as a cross-check.

The expected top-squark pair production cross section decreases from approximately 19 pb for $m_{\tilde{t}} = 200$ GeV to 0.008 pb for $m_{\tilde{t}} = 700$ GeV. For light top squarks ($m_{\tilde{t}} \approx m_t$) the production cross section is reasonably large but the main kinematic variables, in particular M_T, are very similar to SM $t\bar{t}$ production. For large top squark masses the kinematic distributions for signal events differ from those from SM $t\bar{t}$ production, but the cross section decreases rapidly, reducing the signal-to-background ratio.

2 Signal and background Monte Carlo simulation

Monte Carlo (MC) simulations of SM processes, as well as signal models with $\tilde{t} \to t\tilde{\chi}_1^0$ or $\tilde{t} \to b\tilde{\chi}_1^+$, are used to design the analysis, to estimate the backgrounds, and to calculate the signal acceptance in the search regions. Event samples for SM processes are generated using the PYTHIA 6.4.22 [24], MADGRAPH 5.1.3.30 [25], MC@NLO [26, 27], or POWHEG [28] MC event generators and the CTEQ6.6 parton density functions [29]. The most important background to the analysis is from SM $t\bar{t}$ events for which we use POWHEG for the "reference" $t\bar{t}$ sample. The MADGRAPH and MC@NLO generators are used for cross-checks and validations. All SM processes are normalized to cross section calculations at next-to-next-to-leading order (NNLO) when available, otherwise at next-to-leading order (NLO) [26, 27, 30–35].

For the signal events, the production of top-squark pairs is generated with MADGRAPH, including up to two additional partons at the matrix-element level. The decays of the top squarks are generated with PYTHIA. A grid of signal events is generated as a function of the top squark and neutralino masses with 25 GeV spacings. For the $\tilde{t} \to b\tilde{\chi}_1^+$ decay mode, the chargino mass is specified by a third parameter x defined as $m_{\tilde{\chi}_1^\pm} = x \cdot m_{\tilde{t}} + (1-x) \cdot m_{\tilde{\chi}_1^0}$. We consider three mass spectra, with $x = 0.25$, 0.50, and 0.75. In the case of $\tilde{t} \to t\tilde{\chi}_1^0$ decays, events with $m_{\tilde{t}} < m_t + m_{\tilde{\chi}^0}$ are also included, where the decay $\tilde{t} \to t\tilde{\chi}^0$ proceeds via off-shell top quarks.

The polarizations of the final and intermediate state particles (top quarks in the $\tilde{t} \to t\tilde{\chi}_1^0$ scenario, and charginos and W bosons in the $\tilde{t} \to b\tilde{\chi}_1^+$ case) are model dependent and are nontrivial functions of the top squark, chargino, and neutralino mixing matrices [36, 37]. The signal MC is chosen to have no polarization. The effect of this choice on our final result will be discussed in Section 8. Expected signal event rates are normalized to cross sections calculated at NLO in the strong coupling constant, including the resummation of soft gluon emission at next-to-leading-logarithmic accuracy (NLO+NLL) [38].

In the MC samples, for both signal and backgrounds, multiple proton-proton interactions in the same or nearby bunch crossings (pileup) are simulated using PYTHIA and superimposed on the hard collision. The simulation of new physics signals is performed using the CMS fast simulation package [39], whereas almost all SM samples are simulated using a GEANT4-based model [40] of the CMS detector. The exceptions are the MADGRAPH $t\bar{t}$ samples used to study the sensitivity of estimated backgrounds to the details of the generator settings; these samples are processed with the fast simulation. The simulated events are finally reconstructed and analyzed with the same software used to process collision data.

3 Event selection

3.1 Object definition and event pre-selection

The data used for this search were collected using single high-p_T isolated electron and muon triggers with p_T thresholds of 27 and 24 GeV, respectively. The muon (electron) trigger efficiency, as measured on a sample of $Z \to \ell\ell$ events, varies between 80% and 95% (85% and 97%) depending on p_T and η. Additionally, data collected with high-p_T double-lepton triggers (ee, eμ, or $\mu\mu$, with p_T thresholds of 17 and 8 GeV on the two leptons), are used for studies of dilepton control regions.

Events are required to have an electron or muon object with $p_T > 25\ (30)$ GeV for muons (electrons). The electrons are required to lie in the barrel region of the electromagnetic calorimeter ($|\eta| < 1.4442$), while the pseudorapidity coverage for muons in this analysis extends to $|\eta| < 2.1$. Muon candidates are reconstructed using an algorithm that performs a global fit requiring consistent hit patterns in the tracker and the muon system [41]. Electron candidates are reconstructed starting from a cluster of energy deposits in the electromagnetic calorimeter. The cluster is then matched to signals in the silicon tracker. A selection using electron identification variables based on shower shape, track-cluster matching, and consistency between the cluster energy and the track momentum is applied to the reconstructed candidates [42].

The particle flow (PF) method [43] is used to reconstruct charged and neutral hadrons, as well as muons, electrons, and photons. Electrons and muons are required to be isolated from other activity in the event. The isolation requirement is constructed from the scalar sum (p_T^{sum}) of the p_T of all PF candidates, excluding the lepton, within a cone of $\Delta R \equiv \sqrt{(\Delta\eta)^2 + (\Delta\phi)^2} < 0.3$ around the lepton direction at the origin. The average contribution of particles from pileup interactions is estimated and subtracted from the p_T^{sum} quantity. The isolation requirement is $p_T^{sum} < \min\{5\text{ GeV}, 0.15 \cdot p_T\}$, where p_T is the transverse momentum of the lepton.

Typical lepton identification and isolation efficiencies, measured in samples of $Z \to \ell\ell$ events, are 91% for muons and 84% for electrons, with variations at the level of a few percent depending on p_T and η. The MC simulation was found to reproduce these efficiencies to within about 2%.

In order to reduce the background from $t\bar{t}$ events in which both W bosons decay leptonically ($t\bar{t} \to \ell^+\ell^-$), events are rejected if they contain indications of an additional lepton: an isolated track with transverse momentum greater than 10 GeV (5 GeV for tracks that are loosely identified as electrons or muons) or a jet with $p_T > 20$ GeV consistent with the hadronic decay of a τ lepton. To reduce the loss in signal acceptance, events with isolated tracks not loosely identified as electrons or muons are rejected only if the track has opposite charge with respect to the selected lepton.

The PF particles are clustered to form jets using the anti-k_T clustering algorithm [44] with a

distance parameter of 0.5, as implemented in the FASTJET package [45, 46]. We apply p_{T}- and η-dependent corrections to account for residual effects of non-uniform detector response. The contribution to the jet energy from pileup is estimated on an event-by-event basis using the jet area method described in Ref. [47], and is subtracted from the overall jet p_{T}. Jets from pileup interactions are suppressed using a multi-variate discriminant based on the multiplicity of objects clustered in the jet, the topology of the jet shape, and the impact parameters of the charged tracks with respect to the signal primary vertex. The jets must be separated from the lepton by $\Delta R > 0.4$ in order to resolve overlaps.

Selected events contain at least four jets with $p_{\mathrm{T}} > 30\,\mathrm{GeV}$ and $|\eta| < 2.4$. At least one of these jets must be consistent with containing the decay of a heavy flavor hadron, as identified by the combined secondary vertex medium working point (CSVM) b-tagging algorithm [48]. We refer to such jets as "b-tagged jets". Additionally, we require $E_{\mathrm{T}}^{\mathrm{miss}} > 100$ GeV.

To summarize, events are required to contain one isolated lepton (e or μ), no additional isolated tracks or hadronic tau candidates, at least four jets with at least one b-tagged jet, and $E_{\mathrm{T}}^{\mathrm{miss}} > 100$ GeV; this is referred to below as the "event pre-selection". Signal regions are then defined by adding the requirement that the transverse mass be greater than 120 GeV. This requirement on M_{T} provides large suppression of the SM backgrounds while retaining high signal efficiency. Requirements on several kinematic quantities (cut-based signal regions, Section 3.3.2) or on the output of the BDT multivariate discriminants (BDT signal regions, Section 3.3.1) are also used to define the signal regions.

3.2 Kinematic quantities

Kinematic requirements, in addition to $M_{\mathrm{T}} > 120$ GeV, are used to enhance sensitivity to top-squark signatures. These requirements are based on kinematic quantities that are found to provide good discrimination between signal and background in MC. The variables used in the definition of the signal regions (see Section 3.3) are described in Sections 3.2.1- 3.2.4. The distributions of the kinematic quantities used in this search after the pre-selection are shown in Figs. 2 and 3. These quantities are found to be well modeled in simulation.

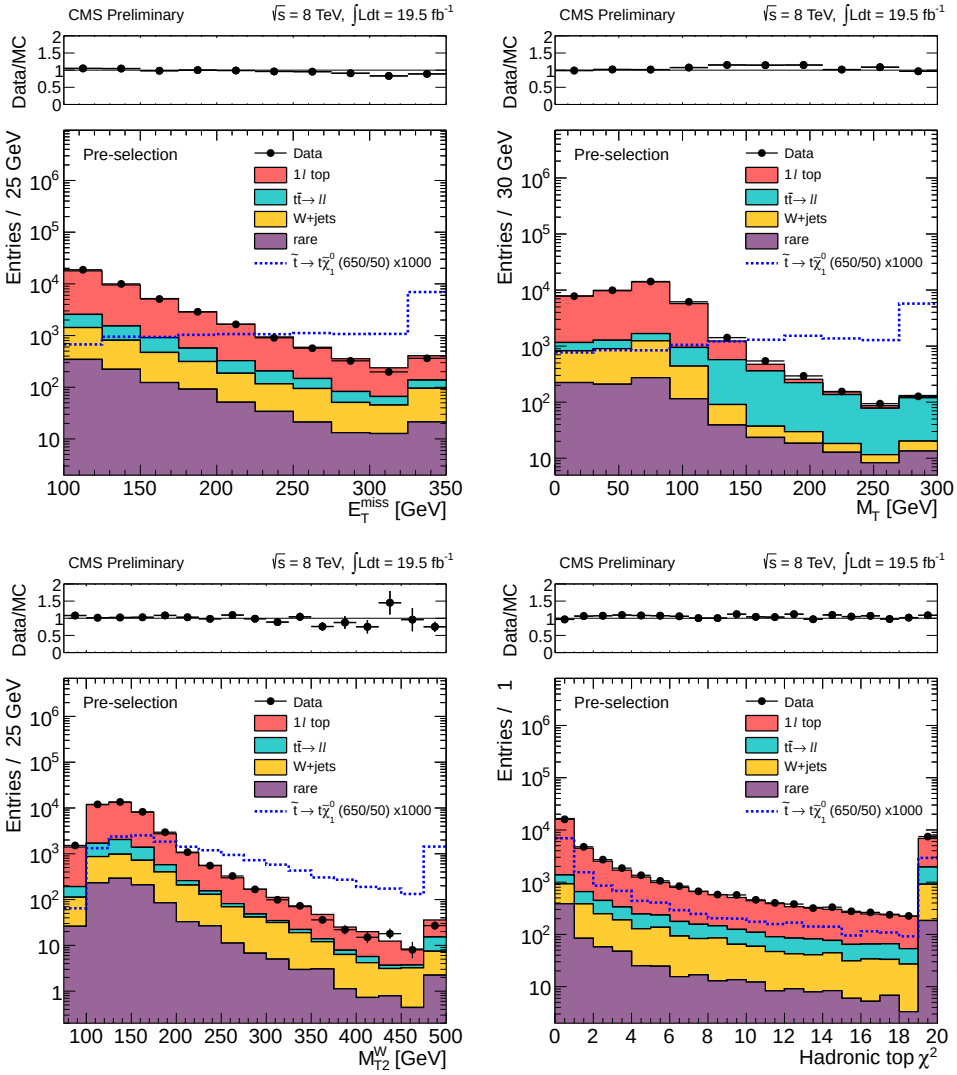

Figure 2: Data vs. MC simulation comparisons of the kinematical quantities discussed in Section 3.2, after the event pre-selection. The $E_{\mathrm{T}}^{\mathrm{miss}}$, M_{T}, $M_{\mathrm{T2}}^{\mathrm{W}}$, and hadronic top χ^2, are indicated. The distributions for the $\tilde{\mathrm{t}} \to \mathrm{t}\tilde{\chi}_1^0$ model with $m_{\tilde{t}} = 650\,\mathrm{GeV}$ and $m_{\tilde{\chi}_1^0} = 50\,\mathrm{GeV}$, scaled by a factor of 1000, are overlaid. In all distributions, the last bin contains the overflow.

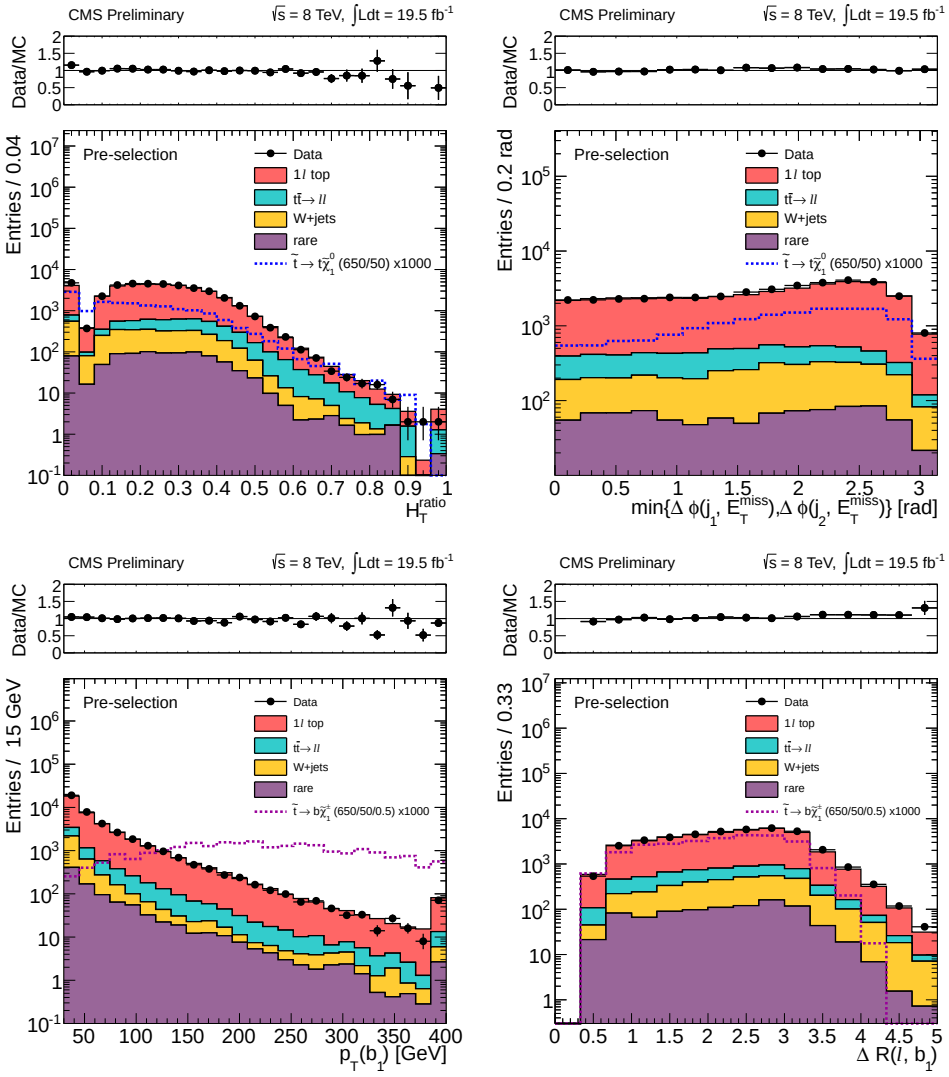

Figure 3: Data vs. MC simulation comparisons of the kinematical quantities discussed in Section 3.2, after the event pre-selection. The $H_{\mathrm{T}}^{\mathrm{ratio}}$, minimum $\Delta\phi$ between the $E_{\mathrm{T}}^{\mathrm{miss}}$ and the two leading jets, p_{T} of the leading b-tagged jet, and the ΔR between the leading b-tagged jet and the lepton are indicated. The distributions for the $\tilde{\mathrm{t}} \rightarrow \mathrm{t}\tilde{\chi}_1^0$ model with $m_{\tilde{t}} = 650\,\mathrm{GeV}$ and $m_{\tilde{\chi}_1^0} = 50\,\mathrm{GeV}$ (top) and $\tilde{\mathrm{t}} \rightarrow \mathrm{b}\tilde{\chi}_1^+$ model with $m_{\tilde{t}} = 650\,\mathrm{GeV}$, $m_{\tilde{\chi}_1^0} = 50\,\mathrm{GeV}$ and $x = 0.5$ (bottom), scaled by a factor of 1000, are overlaid. In all distributions, the last bin contains the overflow.

3.2.1 The M_{T2}^{W} variable

To reduce the dominant $t\bar{t} \to \ell^+\ell^-$ background, we make use of the quantity M_{T2}^{W}, originally defined in Ref. [49]. Fig. 4 is a sketch of a $t\bar{t} \to \ell^+\ell^-$ background event, with dashed lines representing unseen particles. In contrast to a $t\bar{t} \to \ell +$ jets event, the sketched event can easily satisfy the E_T^{miss} and M_T requirements because of the missing energy contributed by the additional neutrino and the unseen lepton. In this case, M_T is not bounded by the W mass.

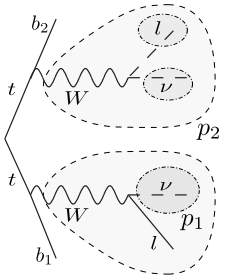

Figure 4: Schematic of M_{T2}^{W} for a dilepton $t\bar{t}$ event [49]. Here p_2 is the four-momentum of the entire missing on-shell W and p_1 is the four-momentum of the neutrino that gets paired with the visible lepton to form the other on-shell W. The dashed lines represent unseen particles, the solid lines indicate reconstructed particles. and the dotted line surround the lepton-neutrino pairs that are constrained to have a mass equal to that of the W boson.

The M_{T2}^{W} quantity is defined as the minimum "mother" particle mass compatible with all the transverse momenta and mass-shell constraints (the neutrinos are massless, and the W bosons are treated as on-shell), according to:

$$M_{T2}^{W} = \text{minimum} \left\{ m_y \text{ consistent with: } \left[\begin{array}{r} \vec{p}_1^{\,T} + \vec{p}_2^{\,T} = \vec{E}_T^{miss}, p_1^2 = 0, (p_1 + p_l)^2 = p_2^2 = M_W^2, \\ (p_1 + p_l + p_{b_1})^2 = (p_2 + p_{b_2})^2 = m_y^2 \end{array} \right] \right\}. \tag{1}$$

By construction, for the dilepton $t\bar{t}$ background without mismeasurement effects, M_{T2}^{W} has an endpoint at the top mass. However, the M_{T2}^{W} calculation relies on the correct identification of the bjets and the correct pairing of the bjets with the leptons. Thus, we extend the M_{T2}^{W} definition as the minimum of the M_{T2}^{W} values calculated from all possible combinations of b-jets and lepton. For events with only one b-tagged jet, the combinations are made using each of the three remaining highest p_T jets as the possible second b-jet.

3.2.2 Hadronic top χ^2

In the $\tilde{t} \to t\tilde{\chi}_1^0$ search, the $t\bar{t}$ dilepton background is suppressed by demanding that three of the jets in the event be consistent with $t \to bW \to bq\bar{q}$. For each triplet of jets in the event we construct a χ^2 as:

$$\chi^2 = \frac{(M_{j_1j_2j_3} - M_{\text{top}})^2}{\sigma^2_{j_1j_2j_3}} + \frac{(M_{j_1j_2} - M_W)^2}{\sigma^2_{j_1j_2}}. \tag{2}$$

Here $M_{j_1j_2j_3}$ is the mass of the 3-jet system, $M_{j_1j_2}$ is the mass of two of the jets posited to originate from W boson decay, and $\sigma_{j_1j_2j_3}$ and $\sigma_{j_1j_2}$ are the uncertainties on these masses calculated from the jet energy resolutions. Finally, $M_{\text{top}} = 173.5\,\text{GeV}$ ($M_W = 80.4\,\text{GeV}$) is the mass of the

top quark (W boson) [50]. The jet assignments are made consistently with the b-tagging information, and the three jets are required to have $p_T > 30$ GeV and $|\eta| < 2.4$ and to be amongst the six leading selected jets. The 3-jet mass $M_{j_1 j_2 j_3}$ is computed after requiring $M_{j_1 j_2} = M_W$ using a constrained kinematic fit. An event-by-event discriminant is then taken as the minimum χ^2 amongst all possible combinations.

3.2.3 Topological variables

Two topological variables are used in the selection of signal candidates. The first is the minimum $\Delta\phi$ between the E_T^{miss} vector and either of the two highest p_T jets, referred to below as "min $\Delta\phi$". Background $t\bar{t}$ events tend to have high p_T top quarks and objects in these events tend to be collinear in the transverse plane. The second variable is H_T^{ratio}, defined as the fraction of the scalar sum of the jet transverse energies (H_T) in the same hemisphere as the E_T^{miss} vector. This quantity tends to be smaller for signal than for background events, because the visible particles may recoil against the LSPs and lead to visible energy in the opposite hemisphere as the E_T^{miss}.

3.2.4 b-quark kinematics

In the $\tilde{t} \to b\tilde{\chi}_1^+$ decay mode, the bottom quarks arise from the decay of the top squark, while in background events they originate from the decay of the top quark. As a result, in most of the signal parameter space the p_T spectrum of the bottom quarks is higher for the signal than for the background. In the $\tilde{t} \to t\tilde{\chi}_1^0$ decay mode, when the top quark in the decay $\tilde{t} \to t\tilde{\chi}_1^0$ is off-shell, the p_T spectrum of the bottom quarks is softer for signal than for the background. The p_T of the highest p_T b-tagged jet is therefore a useful discriminant. An additional, related, discriminating variable is the ΔR separation between this jet and the lepton.

3.3 Signal Region Definition

Two approaches have been pursued to define the signal regions (SRs): a cut-based approach and a BDT multivariate approach. In both approaches, we apply the pre-selection requirements of Section 3.1. The cut-based signal regions are then defined by adding requirements on a set of individual kinematic variables. In contrast, the BDT combines the kinematic variables into a single discriminant, and the BDT SRs are defined by requirements on this discriminant. The BDT approach improves the sensitivity of the search by up to 40%, despite adding some complexity. The primary result of our search is obtained with the BDT, while the cut-based analysis serves as a cross-check.

Table 1 summarizes the requirements for the cut-based SRs and lists the variables used in the training of the BDTs. The BDTs are described in Section 3.3.1. The cut-based selections are discussed further in Section 3.3.2.

3.3.1 BDT signal regions

The primary results of our analysis are based on signal regions that include requirements on the outputs of BDT multivariate discriminators. The BDTs are trained on samples of MC signal and background events satisfying the pre-selection requirements and with $M_T > 120$ GeV. The BDTs were trained with MADGRAPH signal samples for $\tilde{t} \to t\tilde{\chi}_1^0$ and PYTHIA signal samples for $\tilde{t} \to b\tilde{\chi}_1^+$ (the choice of generators has little impact on the final result). The background MC sample contains all the expected SM processes, which are weighted by their respective cross sections.

Selection	$\tilde{t} \to t\tilde{\chi}_1^0$ cut-based Low ΔM	$\tilde{t} \to t\tilde{\chi}_1^0$ cut-based High ΔM	$\tilde{t} \to t\tilde{\chi}_1^0$ BDT	$\tilde{t} \to b\tilde{\chi}_1^+$ cut-based Low ΔM	$\tilde{t} \to b\tilde{\chi}_1^+$ cut-based High ΔM	$\tilde{t} \to b\tilde{\chi}_1^+$ BDT
E_T^{miss}(GeV)	> 150,200, 250,300	> 150,200, 250,300	yes	> 100,150, 200,250	> 100,150, 200,250	yes
M_{T2}^W (GeV)		> 200	yes		>200	yes
min $\Delta\phi$	> 0.8	> 0.8	yes	> 0.8	> 0.8	yes
H_T^{ratio}			yes			yes
χ^2	<5	<5	(on-shell top)			
leading b-jet p_T (GeV)			(off-shell top)		> 100	yes
$\Delta R(\ell$,leading b-jet)						yes

Table 1: Summary of the variables used as inputs for the BDTs and of the kinematic requirements in the cut-based analysis. All signal regions include the requirement $M_T > 120$ GeV. For the $\tilde{t} \to t\tilde{\chi}_1^0$ BDT trained in region 5 where the top quark is off-shell, the hadronic top χ^2 is not included and the leading b-jet p_T is included.

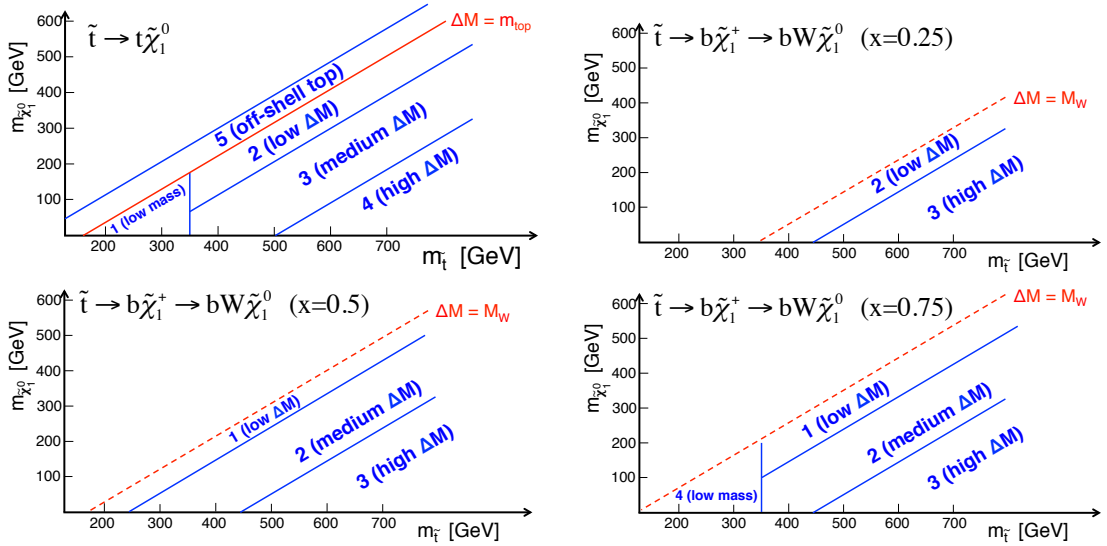

Figure 5: The regions used to train the BDTs, in the $m_{\tilde{\chi}_1^0}$ vs. $m_{\tilde{t}}$ parameter space. $\tilde{t} \to t\tilde{\chi}_1^0$: top left. $\tilde{t} \to b\tilde{\chi}_1^+$, $x = 0.25$ (top right), $x = 0.5$ (bottom left), and $x = 0.75$ (bottom right). The dashed lines correspond to $\Delta M \equiv m_{\tilde{t}} - m_{\tilde{\chi}_1^0} = m_t$ for $\tilde{t} \to t\tilde{\chi}_1^0$, and $\Delta M \equiv m_{\chi_1^+} - m_{\tilde{\chi}_1^0} = m_W$ for $\tilde{t} \to b\tilde{\chi}_1^+$.

Separate BDTs are trained for the $\tilde{t} \to t\tilde{\chi}_1^0$ and $\tilde{t} \to b\tilde{\chi}_1^+$ decay modes and for regions with different signal kinematics. The $\tilde{t} \to t\tilde{\chi}_1^0$ and $\tilde{t} \to b\tilde{\chi}_1^+$ signal parameter spaces are divided into regions with similar kinematics, and one BDT is trained per region. The regions are defined in Fig. 5; the variables used in the BDTs are listed in Table 1.

The BDT operating points, i.e. the requirements on the BDT output used to define each signal region, are selected through an optimization procedure. For each BDT, and each point in the signal parameter space, a figure-of-merit (FOM) is defined as a function of the BDT requirement. The FOM is defined as $S/\sqrt{B + f_B^2 B^2}$, where the S (B) is the expected number of signal (background) events, and $f_B = 0.3$ is a typical relative systematic uncertainty on the background estimate.

In general, for a given BDT, the requirement that maximizes the FOM does not depend strongly

on the point in parameter space within each region. Thus, for almost all regions defined in Fig. 5, a single BDT requirement is sufficient, and each such requirement defines a BDT signal region. The exceptions are Region 1 for the $\tilde{t} \to t\tilde{\chi}_1^0$ case and Region 2 for the $\tilde{t} \to b\tilde{\chi}_1^+$ signal model with parameter $x = 0.5$; in these regions we choose two BDT operating points, a "tight" one and a "loose" one.

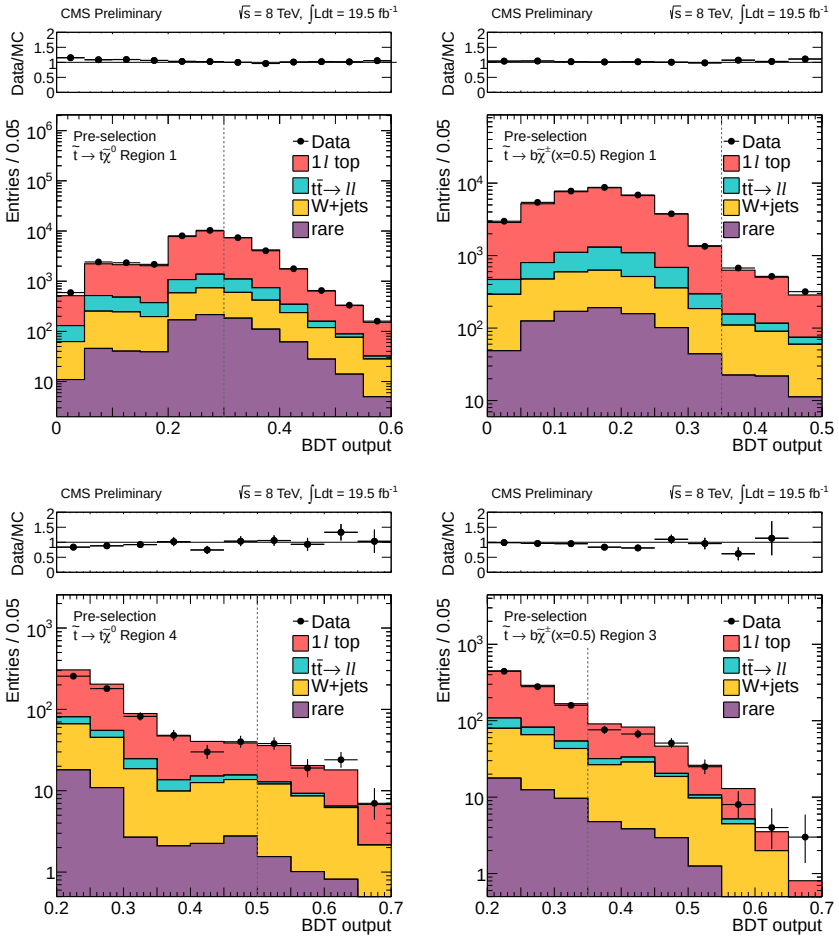

Figure 6: Data vs. MC simulation comparisons of the BDT output for the $\tilde{t} \to t\tilde{\chi}_1^0$ scenario in training region 1 (top left) and region 4 (bottom left) and the $\tilde{t} \to b\tilde{\chi}_1^+$scenario with $x = 0.5$ in training region 1 (top right) and region 3 (bottom right). The event pre-selection is applied. The vertical dashed line indicates the corresponding signal region requirement. The last bin contains the overflow.

3.3.2 Cut-based signal regions

As a cross-check, we also pursue a "cut-based" analysis with signal regions defined by requirements on several kinematic quantities. For the $\tilde{t} \to t\tilde{\chi}_1^0$ model, two types of signal regions are distinguished: those targeting "small ΔM" and those targetting "large ΔM", where $\Delta M = m_{\tilde{t}} - m_{\tilde{\chi}^0}$. Both categories include the requirement that the azimuthal angular difference between the two leading jets and the E_T^{miss} vector be > 0.8 radians, in addition to the requirement $\chi^2 < 5$. For small ΔM no requirement is applied on M_{T2}^W, due to the large inefficiency from this requirement, while for large ΔM we require $M_{T2}^W > 200$ GeV. Within each set, the signal regions are distinguished by four successively tighter E_T^{miss} requirements, $E_T^{miss} > 150, 200, 250$ and 300 GeV.

For the $\tilde{t} \to b\tilde{\chi}_1^+$ model, the same approach is followed as for $\tilde{t} \to t\tilde{\chi}_1^0$ by defining two sets of signal regions, one for small ΔM and one for high ΔM, where ΔM here is the mass difference between the chargino and the LSP. Just as in the $\tilde{t} \to t\tilde{\chi}_1^0$ case, SRs are distinguished by increasingly tighter requirements on E_T^{miss}. Since in the case of $\tilde{t} \to b\tilde{\chi}_1^+$ the signal has no top quark in its decay products, the requirement on the hadronic χ^2 is not used. The large ΔM selection includes the M_{T2}^W requirement, as well as the requirement that the leading b-tagged jet satisfy $p_T > 100$ GeV.

3.3.3 Signal regions summary

To summarize, this search uses two complementary approaches, cut-based and BDT multivariate. As a result, there are two distinct sets of signal regions, cut-based and BDT, where in the case of the BDT approach the SRs are defined by requirements on the BDT outputs. The BDT SRs provide the primary result, since the BDT method has better sensitivity. There are a total of 16 cut-based SRs (8 each for the $\tilde{t} \to t\tilde{\chi}_1^0$ and $\tilde{t} \to b\tilde{\chi}_1^+$ cases), as well as 16 BDT SRs (6 for the $\tilde{t} \to t\tilde{\chi}_1^0$ mode and 10 for the $\tilde{t} \to b\tilde{\chi}_1^+$ case).

The large number of SRs is necessary to target the two possible decay modes ($\tilde{t} \to t\tilde{\chi}_1^0$ vs. $\tilde{t} \to b\tilde{\chi}_1^+$) and to maintain sensitivity over a wide range of SUSY mass parameter space. As will be discussed in Section 7, the expected number of background events in the SRs varies between approximately 1600 and 4. In general, the looser SRs are sensitive to light top squarks that are produced with high cross section but are difficult to distinguish from the $t\bar{t}$ background. In contrast, the tighter SRs are sensitive to high mass top squarks that have low production cross section but more distinct kinematic properties.

BDT distributions after the pre-selection for four out of the 16 BDTs are shown in Fig. 6. The data are in good agreement with the SM MC simulation at this stage of the analysis.

4 Backgrounds and estimation methodology

This section presents an overview of the backgrounds and the methods used to estimate them. The SM background is divided into four categories that are evaluated separately. The largest background contribution is $t\bar{t}$ production in which both W bosons decay leptonically ($t\bar{t} \to \ell^+\ell^-$), but one of the leptons is not identified. The second largest background consists of $t\bar{t}$ production in which one W boson decays leptonically and the other hadronically ($t\bar{t} \to \ell + \text{jets}$), as well as single-top production in the s-channel and t-channel modes. These are collectively referred to as "single-lepton top" processes. The third largest background consists of a variety of SM processes with small cross section, including $t\bar{t}$ events produced in association with a vector boson ($t\bar{t}W$, $t\bar{t}Z$, $t\bar{t}\gamma$), processes with two (WW, WZ, ZZ) and three (WWW, WWZ, WZZ, ZZZ) electroweak vector bosons, and single-top production in the tW-channel mode. These procesess are collectively referred to as the "rare" processes. The production of Z bosons in association with jets (Z+jets) is also included in this category. Although the cross section for this process is quite large, this background is strongly suppressed by the E_T^{miss} requirement and by the requirements placed on the number of jets and b-tagged jets. As a result its contribution in the signal regions is very small. The fourth and final background contribution is from the production of W bosons with jets (W+jets). The multijet contribution to the background is negligible in the signal regions due to the requirement of a high-p_T isolated lepton, large M_T large E_T^{miss}, and the presence of a b-tagged jet.

All backgrounds are estimated from simulated events. The simulation is validated in control regions (CRs) designed to enrich the data sample in specific sources of background while main-

taining kinematical properties that are similar to those in the signal regions. This validation is described in detail in Section 5. In these regions the kinematical variables used in the cut-based and BDT selections are examined to verify that they are properly modeled. A key distribution in each CR is that of M_{T} after the cut-based or BDT selection requirements. The data/MC comparison of the number of events with $M_{\mathrm{T}} > 120$ GeV is a direct test of the ability of the method to correctly predict the SM background in the signal regions. The CR studies were designed to extract data/MC scale factors to be applied to the MC predictions for the background in the signal regions. We find that only one such scale factor needs to be applied. This is a scale factor related to an underestimation of the M_{T} tail for single-lepton top and W+jets, see Section 5.3.

The signal selections require at least four hadronic jets. As mentioned above, the dominant background consists of $\mathrm{t\bar{t}} \to \ell^+\ell^-$ events with one unidentified lepton. These events can satisfy the signal region selection only if there are two additional jets from initial- or final-state radiation (ISR/FSR), or one such jet in conjunction with a second lepton identified as a jet (e.g. in the case of hadronic tau decays). Thus, any mismodeling of the jet multiplicity in the $\mathrm{t\bar{t}}$ simulation would introduce a bias in the $\mathrm{t\bar{t}} \to \ell^+\ell^-$ background prediction. To check this effect, a data control sample dominated by $\mathrm{t\bar{t}} \to \ell^+\ell^-$ events is defined by requiring the presence of exactly two opposite-sign leptons (electrons or muons) in events satisfying dilepton triggers. To suppress the Z+jets background, same-flavor (ee or $\mu\mu$) events with an invariant mass in the range $76 < m_{\ell\ell} < 106$ GeV are rejected, the presence of at least one b-tagged jet is required, and minimum requirements are imposed on $E_{\mathrm{T}}^{\mathrm{miss}}$. We then compare the distribution of the number of jets (N_{jets}) in data vs. MC simulation, as displayed in Fig. 7, to determine how well the simulation describes the measured $\mathrm{t\bar{t}} \to \ell^+\ell^-$ rate when there are three or more jets in the event. The fraction of $\mathrm{t\bar{t}} \to \ell^+\ell^-$ events with three or four or more jets is found to be in agreement with the expectation from the MC simulation within a 3% statistical uncertainty.

In order to minimize systematic uncertainties due to $\mathrm{t\bar{t}}$ production cross section, integrated luminosity, lepton efficiency, and jet energy scale, the $\mathrm{t\bar{t}}$ MC backgrounds are always normalized to the number of events in data in the transverse mass peak region, defined as $50 < M_{\mathrm{T}} < 80$ GeV, and then extrapolated to the tail of M_{T}. For each cut-based or BDT signal region, we select events passing all the requirements except that the $M_{\mathrm{T}} > 120$ GeV requirement is replaced

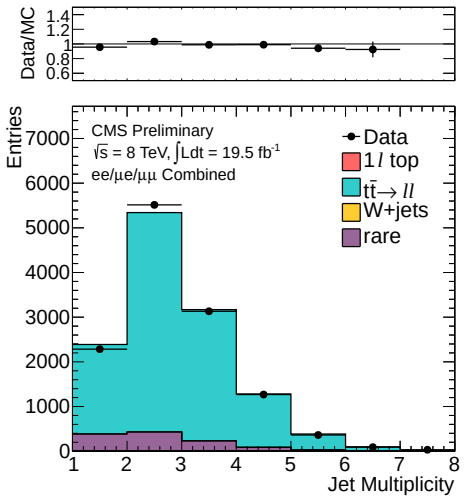

Figure 7: Comparison of the jet multiplicity distributions in data and MC simulation for the sample dominated by $\mathrm{t\bar{t}} \to \ell^+\ell^-$events, as discussed in Sec. 4.

by the requirement $50 < M_{\mathrm{T}} < 80$ GeV, yielding a sample that is dominated by single-lepton top and W+jets events. First, the $\mathrm{t\bar{t}}$ and W+jets samples are normalized to data in the M_{T} peak region, after imposing all requirements except for the rejection of events with an isolated track or a hadronic tau candidate. Second, the isolated track veto and the tau veto are imposed and a second scaling factor is applied to the single lepton backgrounds only (single-lepton top and W+jets backgrounds) such that the total MC yield matches the data in the M_{T} peak region. This procedure corrects for potential differences in the isolated track and hadronic tau misidentification rates in the data vs. MC simulation. Here we rely on the fact that the efficiency to identify genuine isolated leptons is well modeled in MC, which is verified through studies of $\mathrm{Z} \to \ell\ell$ events in data and MC. The background predictions are then extrapolated into the M_{T} tail, using the "tail-to-peak ratio" (R) of the number of events with M_{T} satisfying the signal region requirement to the number of events in the M_{T} peak region, separately for the dilepton $\mathrm{t\bar{t}}$, single-lepton top, and W+jets backgrounds.

Background contributions from the processes referred above as "rare" are taken directly from MC simulation. Their rates are normalized using the corresponding NLO cross sections.

5 Control region studies

As discussed in Section 4, we define control regions (CRs) to test the background prediction and to further validate the modeling of the kinematic quantities used in the cut-based and BDT analyses. The CRs have the same requirements as the signal regions (SR), except that the $M_{\mathrm{T}} > 120$ GeV requirement is removed. In addition, the CRs and the SRs differ in the number of b-tagged jets and lepton candidates.

Three CRs are used in this analysis. A sample dominated by $\mathrm{t\bar{t}} \to \ell^+\ell^-$ events is obtained by requiring the presence of two selected leptons (CR-2ℓ, Section 5.1). A sample dominated by a mixture of $\mathrm{t\bar{t}} \to \ell +$ jets and $\mathrm{t\bar{t}} \to \ell^+\ell^-$ events is obtained by requiring the presence of a selected lepton and one isolated track or hadronic tau candidate (CR-ℓt, Section 5.2). A sample dominated by W+jets events is obtained by inverting the requirement of at least one b-tagged jet (CR-0b, Section 5.3).

In all CRs, we apply the various SR selections and we then compare data and MC-predicted yields with $M_{\mathrm{T}} > 120$ GeV, normalized to the M_{T} peak as described in Section 4. The BDT output distribution trained in $\tilde{\mathrm{t}} \to \mathrm{t}\tilde{\chi}_1^0$ Region 1 is shown in Fig. 8 for the three control regions. The M_{T} distributions after the BDT signal region requirement is also displayed in Fig. 8. Similar levels of agreement between data and MC are found for the other SR-like selections.

In the case of CR-2ℓ and CR-ℓt, the number of data events with $M_{\mathrm{T}} > 120$ GeV is consistent with the MC prediction. The level of agreement is used to assess a systematic uncertainty on the $\mathrm{t\bar{t}} \to \ell^+\ell^-$ background prediction. The uncertainty ranges from 5% for the loosest signal regions to 70% for the tightest signal regions, reflecting the limited statistical precision of the control samples after the M_{T} and BDT requirements are applied.

In the case of CR-0b we find that the M_{T} tail in W+jets events is somewhat underestimated by the simulation. The results of the CR-0b study are then used to correct the MC predictions of the W+jets and single-lepton top backgrounds. This procedure is discussed further in Section 5.3.

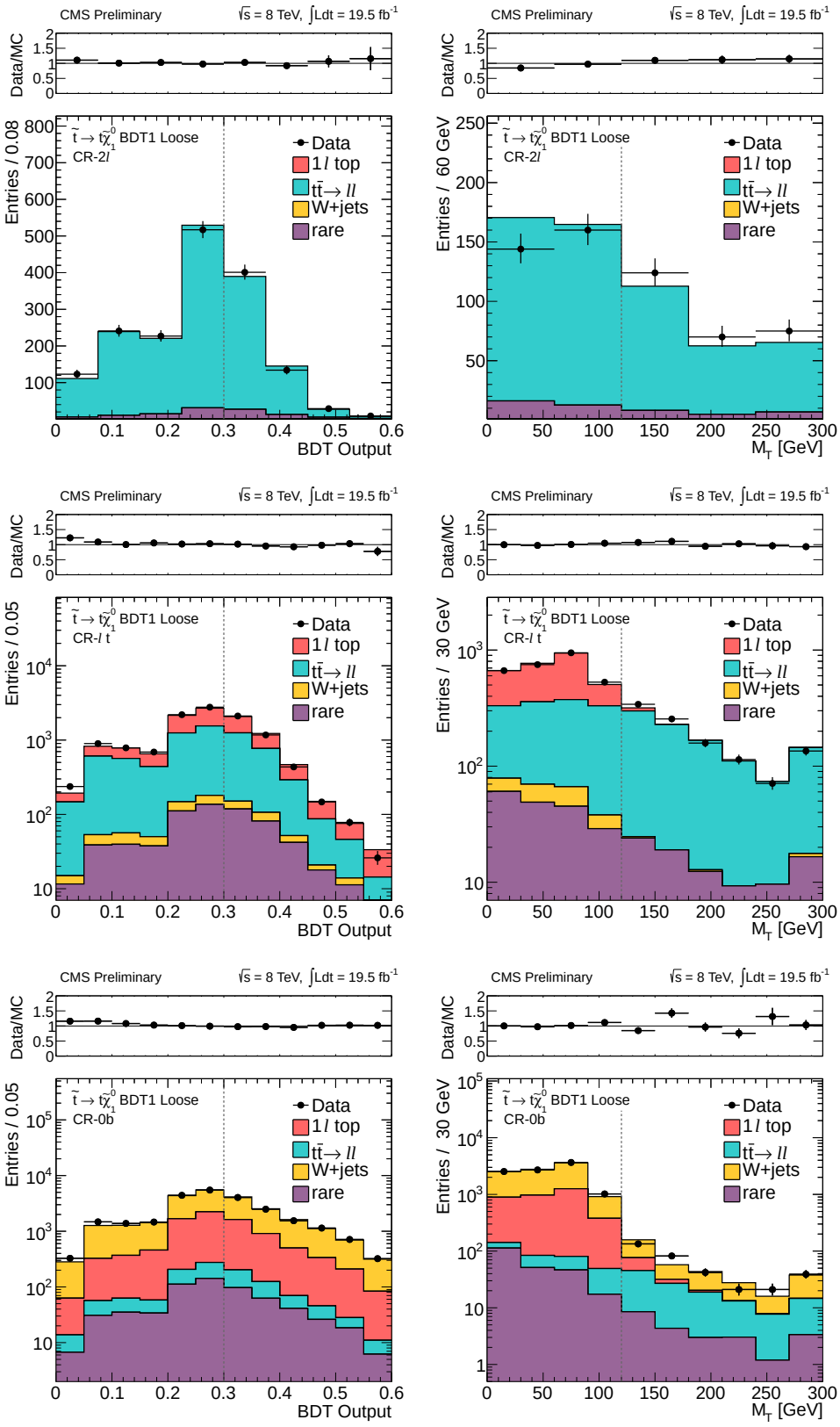

Figure 8: Data vs. MC simulation comparisons in the control regions CR-2ℓ (top row), CR-ℓt (middle row), and CR-0b (bottom row) of the BDT output distribution for the $\tilde{t} \to t\tilde{\chi}_1^0$ model in training region 1 (left) and the corresponding M_T distribution (right) after the signal-like requirement on the BDT output (indicated by the dashed line). For the plots in CR-0b, the scale factors are applied to the MC in the M_T tail. In all plots, the last bin contains the overflow.

5.1 CR-2ℓ: exactly 2 leptons and $\geq$1 b-tag

This CR consists of events with exactly two selected leptons and at least one b-tagged jet. The contribution from $Z \to \ell\ell$ events is removed by an invariant mass veto in the ee and $\mu\mu$ channels. The definition of M_{T} in this control region is ambiguous because there are two leptons. We construct M_{T} from the leading lepton and the $E_{\mathrm{T}}^{\mathrm{miss}}$. As mentioned above, a sample M_{T} distribution in this control region after BDT requirements is shown in Fig. 8.

5.2 CR-ℓt: 1 lepton + 1 isolated track or tau candidate and $\geq$ 1 b-tag

Events in CR-ℓt are those that satisfy all selection requirements but fail the second lepton veto, either the isolated track veto or the hadronic tau veto. This control region consists of $\mathrm{t\bar{t}} \to \ell\ell$ and $\mathrm{t\bar{t}} \to \ell +$ jets events where a jet fluctuates to a single high p_{T} isolated track or is misidentified as a hadronic tau candidate. The $\mathrm{t\bar{t}} \to \ell +$ jets component is significant in the M_{T} peak region, while the events with large M_{T} are dominated by $\mathrm{t\bar{t}} \to \ell^+\ell^-$. The $\mathrm{t\bar{t}}$ and W+jets backgrounds are normalized to the M_{T} peak region in data, following the same procedure described in Section 4. As mentioned above, a sample M_{T} distribution in this control region after BDT requirements are shown in Fig. 8.

5.3 CR-0b: exactly 1 lepton, 0 b-tags

The full event selection is applied to events in this CR, including the isolated track veto and the tau veto, but requiring zero b-tags. With zero b-tagged jets and one lepton, this region is dominated by W+jets events. As an initial test, we determine the scale factor needed to match the MC and data in the M_{T} peak region $50 < M_{\mathrm{T}} < 80\,\mathrm{GeV}$, and verify that it does not deviate significantly from 1.

However, the transverse mass distribution of these events exhibits a small excess at high M_{T} with respect to the MC prediction. This discrepancy is attributed to imperfect modeling of the tails of the $E_{\mathrm{T}}^{\mathrm{miss}}$ resolution in lepton + jets events. The data/MC agreement in the CR-0b M_{T} tail can be restored by rescaling the W+jets contribution by a factor of 1.2 ± 0.3, as seen for example in Fig. 8, bottom right. We find that this factor is consistent with being the same, within the statistical uncertainties, for all CRs. It is therefore applied to the W+jets background prediction everywhere.

The fact that the simulation underestimates the M_{T} tail in the W+jets sample suggests that a similar effect should exist in the single-lepton top background. However, the M_{T} tail is larger for the W+jets background than for the single-lepton top background, due to a significant contribution of very off-shell W bosons to the tail of the M_{T} distribution in W+jets events. This contribution is not present for the single lepton top background since the lepton-neutrino mass $m_{\ell\nu}$ cannot exceed the difference between the top- and bottom-quark masses, $m_{\ell\nu} < m_{\mathrm{t}} - m_{\mathrm{b}}$. For this reason the scale factor of 1.2 ± 0.3 measured in W+jets cannot be simply applied to the single-lepton top sample.

The tail-to-peak ratio of the W+jets sample ($R_{\mathrm{W+jets}}$), measured in simulation and corrected using the scale factor above, constitutes an upper bound for the tail-to-peak ratio of the single-lepton top background (R_{top}). A lower bound is formed by measuring R_{top} in simulation and applying the same CR-0b scale-factor (which is an underestimate due to the larger contribution to the M_{T} tail from resolution effects in single-lepton top events). Since the true value of R_{top} lies between these two extremes, we take the average of the upper and lower bounds. The uncertainty includes the statistical uncertainty in the data/MC scale factor from CR-0b, and half the difference between these upper and lower bounds.

6 Systematic uncertainties on the background prediction

In this section we summarize the systematic uncertainties on the predicted backgrounds from $t\bar{t} \to \ell^+\ell^-$, single-lepton top, rare, and W+jets processes.

All backgrounds except for the rare contribution are normalized to data in the M_T peak region, so the statistical uncertainties in the data and MC yields in the M_T peak region contribute to the background predictions in the high M_T signal regions. This normalization is repeated after varying the W+jets background yield in the M_T peak region by $\pm 50\%$ to estimate the associated systematic uncertainty.

For the $t\bar{t} \to \ell^+\ell^-$ background, the dominant uncertainty is assessed based on the data/MC comparison in the high-M_T regions of CR-2ℓ and CR-ℓt after applying the kinematic requirements for the corresponding signal region. This uncertainty varies between 5% and 70%, see Section 5.1. The uncertainty in the modeling of additional jets from radiation for the $t\bar{t} \to \ell\ell$ background, described in Section 4, results in a 3% uncertainty on the dilepton background. The uncertainty from the limited number of events in the $t\bar{t} \to \ell^+\ell^-$ MC sample also contributes, particularly in the tight signal regions.

An additional uncertainty is associated with the efficiency to reconstruct a second lepton (e, μ, or 1-prong hadronic τ decay) within the detector acceptance and satisfying the p_T and η requirements of the isolated track veto. We verify that the simulation reproduces this efficiency through studies of $Z \to \ell\ell$ events in data, and we assign a systematic uncertainty of 6%. An uncertainty of 7%, based on studies of the efficiency for tau identification in data and simulation, is applied to events with a hadronic tau in the hadronic tau veto acceptance. We also verify the stability of the $t\bar{t} \to \ell^+\ell^-$ MC background prediction by comparing our nominal POWHEG sample with samples generated with MADGRAPH and MC@NLO, and by varying the MADGRAPH generator parameters Q^2 and matching scale up and down by a factor of 2, and varying the top mass from the nominal value of 172.5 GeV to 178.5 and 166.5 GeV. Since the resulting background predictions are consistent within the systematic uncertainties discussed above, we do not assess any additional uncertainty from these tests.

The uncertainty in the W+jets background prediction is dominated by the uncertainty in the tail-to-peak ratios, as determined from data/MC comparisons in the CR-0b control region. The main uncertainty in the single lepton top backgrounds arises from the difference in the tail-to-peak ratios for W+jets and single-lepton top events. Both of these effects are discussed in Section 5.3.

The uncertainty in the rare SM backgrounds is dominated by the 50% uncertainty taken for the cross section. The systematic uncertainties for the $\tilde{t} \to t\tilde{\chi}_1^0$ BDT analysis are summarized in Table 2. The uncertainties for the other signal regions are presented in Appendix A.

7 Results

A summary of the background expectations after applying all the corrections and the corresponding data counts for each of the signal regions is shown in Table 3 for the $\tilde{t} \to t\tilde{\chi}_1^0$ BDT analysis, Table 4 for the $\tilde{t} \to t\tilde{\chi}_1^0$ cut-based analysis, Table 5 for the $\tilde{t} \to b\tilde{\chi}_1^+$ BDT analysis, and Table 6 for the $\tilde{t} \to b\tilde{\chi}_1^+$ cut-based analysis. Fig. 9 presents a data vs. MC comparison of the M_T and BDT output distributions for events satisfying the loosest and tightest $\tilde{t} \to t\tilde{\chi}_1^0$ BDT signal region requirements. The corresponding comparisons for the loosest and tightest $\tilde{t} \to b\tilde{\chi}_1^+$ signal region requirements are presented in Fig. 10. The M_T and BDT output distributions for the other signal regions are presented in Appendix C.

$\tilde{t} \to t\tilde{\chi}_1^0$						
Sample	BDT1 Loose	BDT1 Tight	BDT2	BDT3	BDT4	BDT5
M_T peak data and MC (stat)	1.0	2.1	2.7	5.3	8.7	3.0
$t\bar{t} \to \ell^+\ell^-$ N_{jets} modeling	1.7	1.6	1.6	1.1	0.4	1.7
$t\bar{t} \to \ell^+\ell^-$ (CR-ℓt and CR-2ℓ tests)	4.0	8.2	11.0	12.5	7.2	13.8
2nd lepton veto	1.5	1.4	1.4	0.9	0.3	1.4
$t\bar{t} \to \ell^+\ell^-$ (stat)	1.1	2.8	3.4	7.0	7.4	3.3
W+jets cross section	1.6	2.2	2.8	1.7	2.7	2.2
W+jets (stat)	1.1	1.9	2.0	4.6	10.8	5.2
W+jets SF uncertainty	8.3	7.7	6.8	8.1	9.7	8.6
1-ℓ Top (stat)	0.4	0.8	0.8	1.4	4.4	1.2
1-ℓ Top tail-to-peak ratio	9.0	11.4	12.4	19.6	28.5	9.1
rare cross sections	1.8	3.0	4.0	8.1	15.7	0.7
Total	13.4	17.1	19.3	27.8	38.4	20.2

Table 2: The bottom row of this table shows the relative uncertainty (in percent) on the total background predictions for the $\tilde{t} \to t\tilde{\chi}_1^0$ BDT signal regions. The breakdown of this total uncertainty in its individual components is also shown.

$\tilde{t} \to t\tilde{\chi}_1^0$						
Sample	BDT1 Loose	BDT1 Tight	BDT2	BDT3	BDT4	BDT5
$t\bar{t} \to \ell\ell$	438 ± 37	68 ± 11	46 ± 10	5 ± 2	0.3 ± 0.3	48 ± 13
1ℓ Top	251 ± 93	37 ± 17	22 ± 12	4 ± 3	0.8 ± 0.9	30 ± 12
W+jets	27 ± 7	7 ± 2	6 ± 2	2 ± 1	0.8 ± 0.3	5 ± 2
Rare	47 ± 23	11 ± 6	10 ± 5	3 ± 1	1.0 ± 0.5	4 ± 2
Total	763 ± 102	124 ± 21	85 ± 16	13 ± 4	2.9 ± 1.1	87 ± 18
Data	728	104	56	8	2	76
$\tilde{t} \to t\tilde{\chi}_1^0$ (250/50)	344 ± 20.9	57 ± 8.4	40 ± 6.9	8.7 ± 3.3	< 0.6	46 ± 7.5
$\tilde{t} \to t\tilde{\chi}_1^0$ (650/50)	12 ± 0.2	7.2 ± 0.2	9.8 ± 0.2	6.5 ± 0.2	4.3 ± 0.1	2.9 ± 0.1

Table 3: The result of the search for the $\tilde{t} \to t\tilde{\chi}_1^0$ BDT analysis. For each signal region the individual background contributions, total background, and observed yields are indicated. The uncertainty includes both the statistical and systematic components. The expected yields for two sample signal models are also indicated. The numbers in parentheses indicate the top squark and neutralino masses, respectively. The uncertainty is statistical.

The observed and predicted yields agree in all signal regions within about 1–1.5σ. Therefore, we observe no evidence for top-squark pair production in our data. We note that there is a tendency for the background predictions to lie somewhat above the observed yields. The yields and background predictions in different signal regions, for both the BDT and cut-based analysis, are highly correlated. The interpretation of these results in the context of models of top-squark pair production is presented in Section 8.

Sample	$E_T^{miss} > 150$ GeV	$E_T^{miss} > 200$ GeV	$E_T^{miss} > 250$ GeV	$E_T^{miss} > 300$ GeV
Low ΔM Selection				
$t\bar{t} \to \ell\ell$	131 ± 15	42 ± 7	17 ± 5	5.6 ± 2.5
1ℓ Top	94 ± 47	30 ± 19	9 ± 6	3.1 ± 2.4
W+jets	10 ± 3	5 ± 1	2 ± 1	1.0 ± 0.4
Rare	16 ± 8	7 ± 4	4 ± 2	1.8 ± 0.9
Total	251 ± 50	83 ± 21	31 ± 8	11.5 ± 3.6
Data	227	69	21	9
$\tilde{t} \to t\tilde{\chi}_1^0$ (250/50)	124 ± 8.8	39 ± 4.9	14 ± 2.9	5.6 ± 1.8
$\tilde{t} \to t\tilde{\chi}_1^0$ (650/50)	8.0 ± 0.1	7.2 ± 0.1	6.2 ± 0.1	4.9 ± 0.1
High ΔM Selection				
$t\bar{t} \to \ell\ell$	8 ± 2	5 ± 2	3.2 ± 1.4	1.4 ± 0.9
1ℓ Top	13 ± 6	6 ± 4	3.0 ± 2.2	1.4 ± 1.0
W+jets	4 ± 1	2 ± 1	1.5 ± 0.5	0.9 ± 0.3
Rare	4 ± 2	3 ± 1	1.8 ± 0.9	1.0 ± 0.5
Total	29 ± 7	17 ± 5	9.5 ± 2.8	4.7 ± 1.4
Data	23	11	3	2
$\tilde{t} \to t\tilde{\chi}_1^0$ (250/50)	9.7 ± 2.4	5.0 ± 1.8	1.3 ± 0.9	0.6 ± 0.6
$\tilde{t} \to t\tilde{\chi}_1^0$ (650/50)	4.9 ± 0.1	4.7 ± 0.1	4.3 ± 0.1	3.7 ± 0.1

Table 4: The result of the search for the $\tilde{t} \to t\tilde{\chi}_1^0$ cut-based analysis. For each signal region the individual background contributions, total background, and observed yields are indicated. The uncertainty includes both the statistical and systematic components. The expected yields for two sample signal models are also indicated. The numbers in parentheses indicate the top squark and neutralino masses, respectively. The uncertainty is statistical.

$\tilde{t} \to b\tilde{\chi}_1^+$ x=0.75				
Sample	BDT1	BDT2	BDT3	BDT4
$t\bar{t} \to \ell\ell$	37 ± 5	9 ± 2	3.1 ± 1.3	248 ± 22
1ℓ Top	17 ± 9	6 ± 5	1.6 ± 1.6	188 ± 70
W+jets	4 ± 1	4 ± 1	1.6 ± 0.6	22 ± 6
Rare	4 ± 2	4 ± 2	1.8 ± 0.9	20 ± 10
Total	61 ± 10	22 ± 6	8.1 ± 2.3	478 ± 74
Data	50	13	5	440
$\tilde{t} \to b\tilde{\chi}_1^+$ (250/50/0.75)	68 ± 29	< 6.0	< 6.0	473 ± 77
$\tilde{t} \to b\tilde{\chi}_1^+$ (650/50/0.75)	3.9 ± 0.4	8.4 ± 0.6	6.8 ± 0.6	5.5 ± 0.5
$\tilde{t} \to b\tilde{\chi}_1^+$ x=0.5				
Sample	BDT1	BDT2 Loose	BDT2 Tight	BDT3
$t\bar{t} \to \ell\ell$	40 ± 5	21 ± 4	4 ± 2	6 ± 2
1ℓ Top	24 ± 10	15 ± 7	4 ± 3	4 ± 2
W+jets	5 ± 1	5 ± 1	2 ± 1	3 ± 1
Rare	8 ± 4	8 ± 4	3 ± 1	4 ± 2
Total	77 ± 12	50 ± 9	13 ± 4	17 ± 4
Data	67	35	12	13
$\tilde{t} \to b\tilde{\chi}_1^+$ (250/50/0.5)	66 ± 27	30 ± 20	< 6.0	< 6.0
$\tilde{t} \to b\tilde{\chi}_1^+$ (650/50/0.5)	3.5 ± 0.4	9.5 ± 0.7	5.6 ± 0.5	8.3 ± 0.6
$\tilde{t} \to b\tilde{\chi}_1^+$ x=0.25				
Sample	BDT2		BDT3	
$t\bar{t} \to \ell\ell$	2.2 ± 1.3		1.2 ± 1.0	
1ℓ Top	4.0 ± 1.8		1.5 ± 0.8	
W+jets	2.0 ± 0.7		0.7 ± 0.3	
Rare	1.6 ± 0.8		1.0 ± 0.5	
Total	9.8 ± 2.4		4.4 ± 1.4	
Data	7		2	
$\tilde{t} \to b\tilde{\chi}_1^+$ (450/50/0.25)	11 ± 2.2		5.2 ± 1.5	
$\tilde{t} \to b\tilde{\chi}_1^+$ (600/100/0.25)	7.5 ± 0.8		5.6 ± 0.7	

Table 5: The result of the search for the $\tilde{t} \to b\tilde{\chi}_1^+$ BDT analysis. For each signal region the individual background contributions, total background, and observed yields are indicated. The uncertainty includes both the statistical and systematic components. The expected yields for two sample signal models are also indicated. The numbers in parentheses indicate the top squark mass, neutralino mass, and chargino mass parameter x, respectively. The uncertainty is statistical.

Sample	$E_{\mathrm{T}}^{\mathrm{miss}} > 100$ GeV	$E_{\mathrm{T}}^{\mathrm{miss}} > 150$ GeV	$E_{\mathrm{T}}^{\mathrm{miss}} > 200$ GeV	$E_{\mathrm{T}}^{\mathrm{miss}} > 250$ GeV
Low ΔM Selection				
$\mathrm{t\bar{t}} \to \ell\ell$	875 ± 57	339 ± 23	116 ± 14	40 ± 9
1ℓ Top	658 ± 192	145 ± 70	41 ± 24	14 ± 9
W+jets	59 ± 15	21 ± 5	8 ± 2	4 ± 1
Rare	70 ± 35	33 ± 17	16 ± 8	8 ± 4
Total	1662 ± 203	537 ± 75	180 ± 28	66 ± 13
Data	1624	487	151	52
$\tilde{\mathrm{t}} \to \mathrm{b}\widetilde{\chi}_1^+$ (250/50/0.5)	454 ± 51	168 ± 30	57 ± 17	25 ± 12
$\tilde{\mathrm{t}} \to \mathrm{b}\widetilde{\chi}_1^+$ (650/50/0.5)	14 ± 0.6	13 ± 0.5	11 ± 0.5	8.4 ± 0.4
High ΔM Selection				
$\mathrm{t\bar{t}} \to \ell\ell$	25 ± 5	12 ± 3	7 ± 2	2.9 ± 1.5
1ℓ Top	35 ± 10	15 ± 6	6 ± 3	2.7 ± 1.8
W+jets	9 ± 2	5 ± 1	2 ± 1	1.8 ± 0.6
Rare	9 ± 5	7 ± 3	4 ± 2	2.4 ± 1.2
Total	79 ± 12	38 ± 7	19 ± 5	9.9 ± 2.7
Data	90	39	18	5
$\tilde{\mathrm{t}} \to \mathrm{b}\widetilde{\chi}_1^+$ (250/50/0.5)	45 ± 15.5	29 ± 12.9	8.5 ± 6.1	8.5 ± 6.1
$\tilde{\mathrm{t}} \to \mathrm{b}\widetilde{\chi}_1^+$ (650/50/0.5)	11 ± 0.5	9.8 ± 0.5	8.6 ± 0.4	6.7 ± 0.4

Table 6: The result of the search for the $\tilde{\mathrm{t}} \to \mathrm{b}\widetilde{\chi}_1^+$ cut-based analysis. For each signal region the individual background contributions, total background, and observed yields are indicated. The uncertainty includes both the statistical and systematic components. The expected yields for two sample signal models are also indicated. The numbers in parentheses indicate the top squark mass, neutralino mass, and chargino mass parameter x, respectively. The uncertainty is statistical.

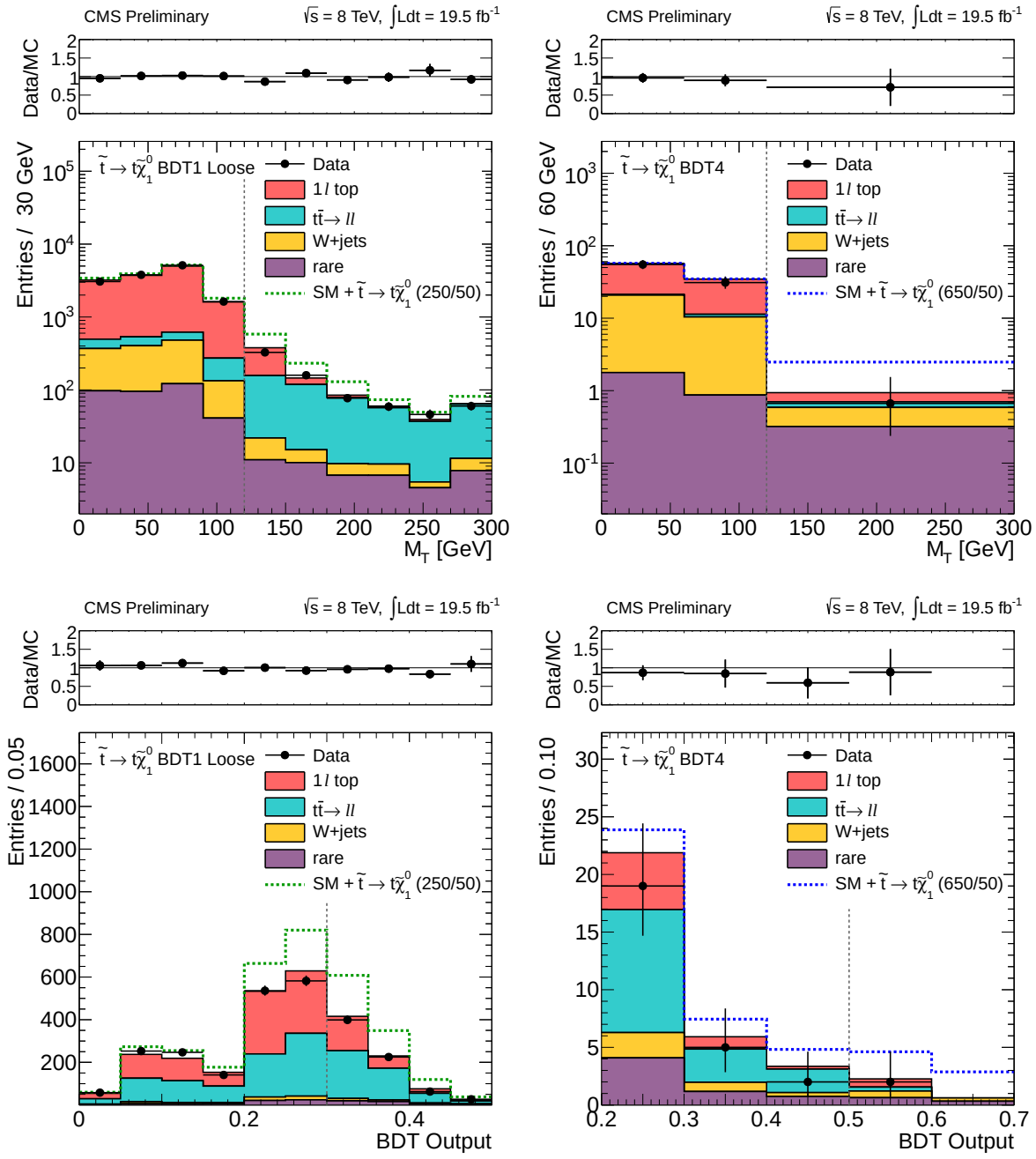

Figure 9: Comparison of the M_{T} (top) and BDT output (bottom) distributions in data vs. MC for events satisfying the loosest (left) and tightest (right) $\tilde{\mathrm{t}} \to \mathrm{t}\tilde{\chi}_1^0$ BDT signal region requirements. In the M_{T} plots, the BDT output signal region requirement is imposed; in the BDT plots, the $M_{\mathrm{T}} > 120$ GeV requirement is imposed. The distributions for the $\tilde{\mathrm{t}} \to \mathrm{t}\tilde{\chi}_1^0$ model with $m_{\tilde{t}} = 250$ GeV and $m_{\tilde{\chi}_1^0} = 50$ GeV (left) and $m_{\tilde{t}} = 650$ GeV and $m_{\tilde{\chi}_1^0} = 50$ GeV (right) are overlaid. The vertical dashed line indicates the corresponding signal region requirement. For the M_{T} distribution after the BDT4 requirement (upper right), the bin to the right of the vertical line contains all events with $M_{\mathrm{T}} > 120$ GeV, and has been scaled by 1/3 to indicate the number of events per 60 GeV.

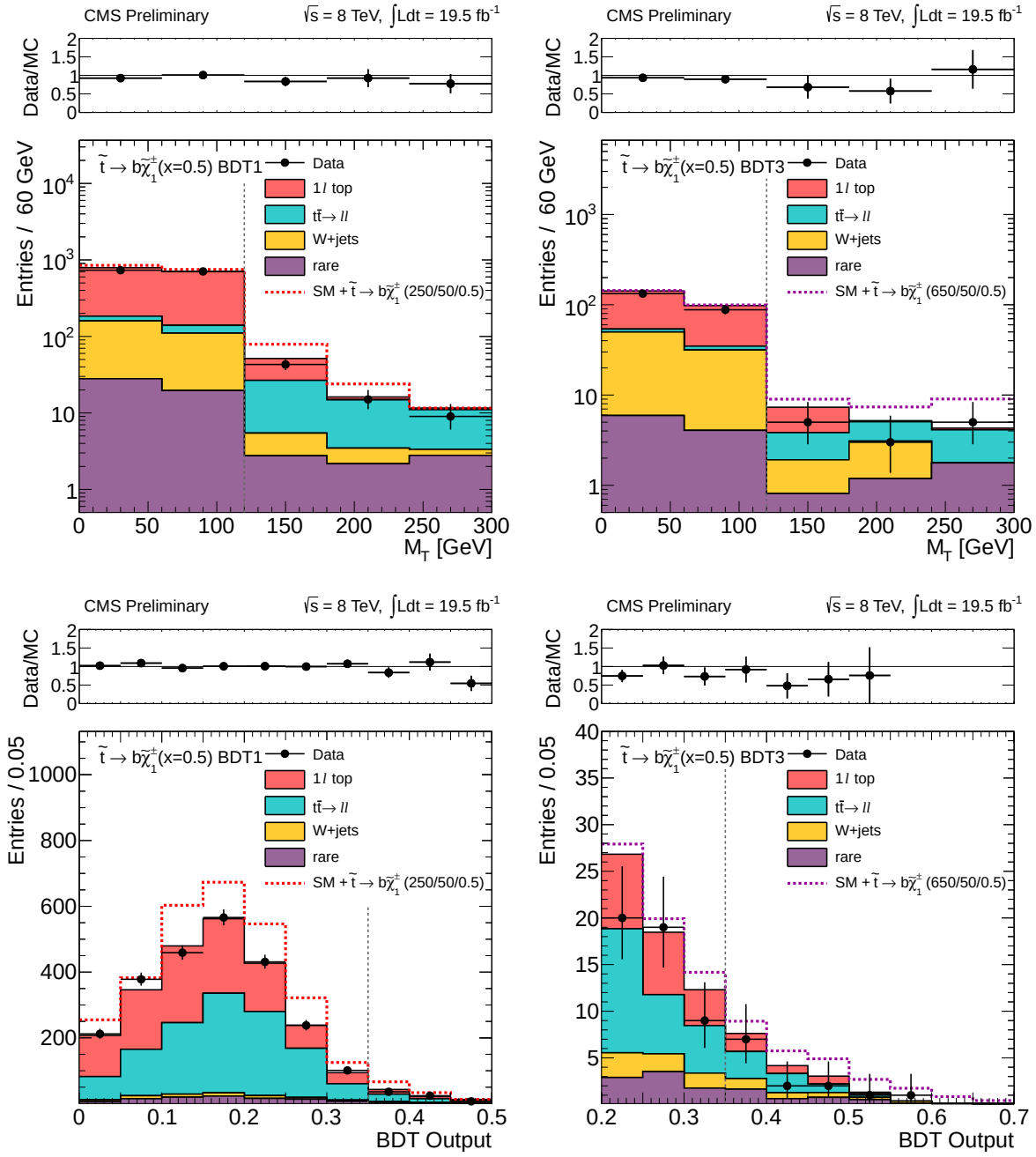

Figure 10: Comparison of the M_{T} (top) and BDT output (bottom) distributions in data vs. MC for events satisfying the loosest (left) and tightest (right) $\tilde{\mathrm{t}} \to \mathrm{b}\tilde{\chi}_1^+$ BDT signal region requirements. In the M_{T} plots, the BDT output signal region requirement is imposed; in the BDT plots, the $M_{\mathrm{T}} > 120$ GeV requirement is imposed. The distributions for the $\tilde{\mathrm{t}} \to \mathrm{b}\tilde{\chi}_1^+$ model with $m_{\tilde{t}} = 250\,\mathrm{GeV}$ and $m_{\tilde{\chi}_1^0} = 50\,\mathrm{GeV}$ (left) and $m_{\tilde{t}} = 650\,\mathrm{GeV}$ and $m_{\tilde{\chi}_1^0} = 50\,\mathrm{GeV}$ (right) are overlaid. The vertical dashed line indicates the corresponding signal region requirement.

8 Interpretation

In this section the results of the search are interpreted in the context of models of top-squark pair production. As discussed in Section 2, we consider two possible decay modes of the top squark, $\tilde{t} \to t\tilde{\chi}_1^0$ and $\tilde{t} \to b\tilde{\chi}_1^+ \to bW\tilde{\chi}_1^0$, each with 100% branching fraction. Using the results of Section 7, we compute 95% confidence level (CL) cross section upper limits limits for top-squark pair production in the $m_{\tilde{\chi}_1^0}$ vs. $m_{\tilde{t}}$ parameter space. Then, based on the expected $pp \to \tilde{t}\bar{\tilde{t}}^*$ production rate, these cross section limits are used to exclude regions of parameter space. For the $\tilde{t} \to b\tilde{\chi}_1^+$ scenario the mass of the intermediate $\tilde{\chi}_1^\pm$ is specified by the parameter x, defined as $m_{\tilde{\chi}_1^\pm} = x m_{\tilde{t}} + (1-x) m_{\tilde{\chi}_1^0}$. We consider three cases: $x = 0.25$, 0.5, and 0.75.

For setting the limit, we account for the following sources of systematic uncertainty in the signal acceptance and efficiency. The uncertainty in the integrated luminosity is 4.4%. The trigger efficiency for events with a selected lepton is measured using samples of $Z \to \ell\ell$ events, with an uncertainty of 3%. The simulated events reproduce the lepton identification and isolation efficiencies measured in data using samples of $Z \to \ell\ell$ to within a few percent. We take a systematic uncertainty of 5% to also account for the modeling of the lepton isolation efficiency in signal events. To account for small differences in the b-tagging efficiencies in data and simulation, the b-tagging discriminator is varied according to its measured uncertainty and propagated to all quantities that depend on b-tagging, resulting in small variations in the signal efficiency that are typically less than 1%. The uncertainty from the jet and E_T^{miss} energy scale is determined separately for each point in the signal model parameter space. The jet transverse energies are varied by their p_T- and $\eta-$dependent uncertainties and used to determine the uncertainty in the selection efficiency for the jet multiplicity, E_T^{miss}, M_T, hadronic top χ^2, and M_{T2}^W requirements. The BDT output is re-evaluated with these varied quantities as inputs. This is the dominant uncertainty in the signal acceptance, and it is largest when the differences between the masses of the top squark and LSP are small. The uncertainty for the signal region with the best sensitivity varies from 3–15% in the model parameter space. In the range of signal efficiency uncertainties relevant in this analysis, the cross section limits depend weakly on the signal efficiency uncertainty. Jets considered in this analysis have scale uncertainties in the range 1–4%.

The experimental acceptance for signals depends on the level of ISR, especially in the small ΔM region where an initial-state boost may be required in order for an event to satisfy the selection requirements, including those on E_T^{miss}, M_T, and the number of reconstructed jets. The modeling of ISR in MADGRAPH is investigated by comparing the predicted p_T spectrum of the system recoiling against the ISR jets to data in Z+jets, $t\bar{t}$, and WZ final states. Good agreement is observed at lower p_T, while the simulation is found to overpredict the data by about 10% at a p_T value of 150 GeV, rising to 20% for $p_T > 250$ GeV. The predictions from the MC signal samples are weighted to account for this difference, by a factor of 0.8–1.0, depending on the p_T of the system recoiling against the ISR jets, and the deviation of this weight from 1 is taken as a systematic uncertainty. Further details are given in Appendix B.

Upper limits on the signal cross section are calculated separately for each signal region, incorporating the uncertainties in the signal acceptance and efficiency discussed above, using the LHC-type CL_s criterion [51–53]. For each point in the signal model parameter space, the observed limit is taken from the signal region with the best expected limit. The results from the BDT analysis are displayed in Fig. 11, for the case when the top quark in $\tilde{t} \to t\tilde{\chi}_1^0$, and the chargino and W-boson in the case of $\tilde{t} \to b\tilde{\chi}_1^+ \to bW\tilde{\chi}_1^0$, are assumed to be unpolarized. The corresponding results from the cut-based analysis, and the most sensitive signal regions for each of the top-squark decay modes, are presented in Appendix D. The cross section limits

from the BDT analysis improve upon those from the cut-based analysis by up to approximately 40%, depending on the model parameters.

Our results probe top squarks with masses between approximately 150 and 650 GeV, for neutralinos with masses up to approximately 250 GeV, depending on the details of the model. For the $\tilde{t} \to t\tilde{\chi}_1^0$ search, the results are not sensitive to the model points with $m_{\tilde{t}} - m_{\tilde{\chi}_1^0} = m_t$, since the $\tilde{\chi}_1^0$ is produced at rest in the top rest frame. However the results are sensitive to model points with $m_{\tilde{t}} - m_{\tilde{\chi}_1^0} < m_t$ and with top squarks lighter than the top, in which the top quark in the decay $\tilde{t} \to t\tilde{\chi}_1^0$ is off-shell.

The signal acceptance depends on the polarization of the intermediate state particles, the top quark in the $\tilde{t} \to t\tilde{\chi}_1^0$ scenario, and the charginos and W bosons in the $\tilde{t} \to b\tilde{\chi}_1^+$ scenario. The polarization of these particles depends on the left/right mixing of the top squarks and on the mixing matrices of the neutralino and chargino [36, 37]. For the $\tilde{t} \to t\tilde{\chi}_1^0$ scenario, the signal sample is generated with unpolarized top quarks. To quantify the impact of this assumption on the mass limits, signal events are reweighted to match the kinematic distributions expected in the pure right-handed and pure left-handed top scenarios. The exclusion regions obtained in the nominal $\tilde{t} \to t\tilde{\chi}_1^0$ scenario with unpolarized top quarks are compared to those obtained with pure left-handed and pure right-handed top quarks in Fig. 12 (left). The limits on the top squark and $\tilde{\chi}_1^0$ masses with pure left-handed or pure right-handed top quarks vary by $\pm$10–20 GeV with respect to the unpolarized top-quark scenario.

In the $\tilde{t} \to b\tilde{\chi}_1^+$ scenario, the signal acceptance depends on the polarization of the chargino, and on whether the $W\tilde{\chi}_1^0\tilde{\chi}_1^\pm$ coupling is left-handed or right-handed. In the signal MC, the decays of the chargino and W boson are generated with flat angular distributions. In the nominal interpretations for the $\tilde{t} \to b\tilde{\chi}_1^+$ models presented in Fig. 11, the signal events are reweighted to reproduce the distributions expected for an unpolarized chargino and left/right-symmetric $W\tilde{\chi}_1^0\tilde{\chi}_1^\pm$ coupling. To quantify the impact of this assumption on the mass limits, the signal events are also reweighted to reproduce the distributions expected for left-handed and right-handed charginos, and for left-handed and right-handed $W\tilde{\chi}_1^0\tilde{\chi}_1^\pm$ couplings. The two scenarios in which the limits deviate the most from our nominal scenario occur for right-handed charginos with right-handed $W\tilde{\chi}_1^0\tilde{\chi}_1^\pm$ coupling (maximum sensitivity) or left-handed $W\tilde{\chi}_1^0\tilde{\chi}_1^\pm$ coupling (minimum sensitivity). The variations in the limits for the $\tilde{t} \to b\tilde{\chi}_1^+$ $x = 0.5$ scenario due to different assumptions about the particle polarizations are displayed in Fig. 12 (right), and the corresponding results for the $x = 0.25$ and $x = 0.75$ scenarios may be found in Appendix D.

9 Summary

We have performed a search for the direct pair production of top squarks, in the final state consisting of a single isolated lepton, jets, large missing transverse energy, and large transverse mass. Signal regions are defined with requirements on the output of a BDT multivariate discriminator, and with requirements on several kinematic discriminants. The observed yields in the signal regions agree with the predicted backgrounds within the assessed uncertainties. The results are interpreted in the context of models of top-squark pair production and decay, and probe top squarks with masses up to about 650 GeV.

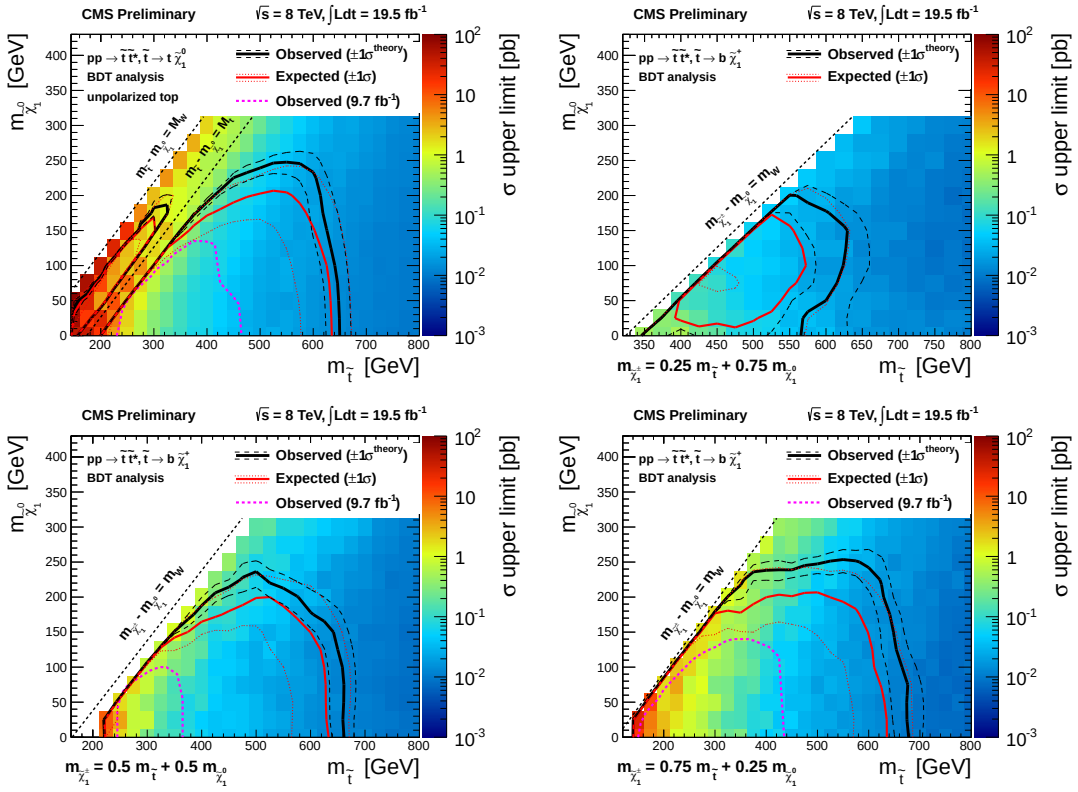

Figure 11: Interpretations using the primary results from the BDT method for the (top left) $\tilde{t} \to t\tilde{\chi}_1^0$ model, and the $\tilde{t} \to b\tilde{\chi}_1^+$ model with chargino mass parameter (top right) $x = 0.25$, (bottom left) $x = 0.5$, and (bottom right) $x = 0.75$. The color scale indicates the observed cross section upper limit. The observed, median expected, and ± 1 standard deviation (σ) expected exclusion contours are indicated.

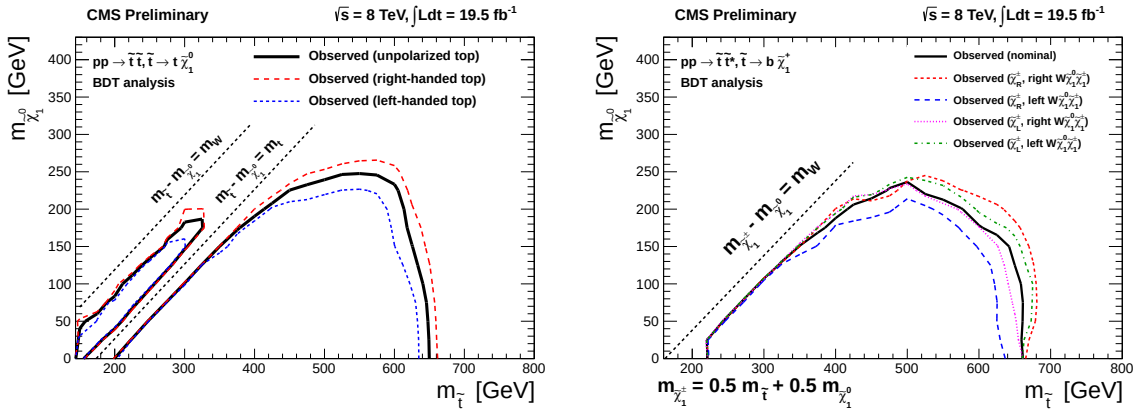

Figure 12: Left: the observed excluded regions for the $\tilde{t} \to t\tilde{\chi}_1^0$ model for the case of unpolarized top quarks, right-handed top quarks, and left-handed top quarks. Right: the observed excluded regions for the $\tilde{t} \to b\tilde{\chi}_1^+$ model with $x = 0.5$ for the nominal scenario, right-handed vs. left-handed charginos ($\tilde{\chi}_R^\pm$ and $\tilde{\chi}_L^\pm$, respectively), and right-handed vs. left-handed $W\tilde{\chi}_1^0\tilde{\chi}_1^\pm$ couplings.

References

[1] S. Dimopoulos and S. Raby, "Supercolor", *Nucl. Phys. B* **192** (1981) 353, doi:10.1016/0550-3213(81)90430-2.

[2] E. Witten, "Dynamical Breaking of Supersymmetry", *Nucl. Phys. B* **188** (1981) 513, doi:10.1016/0550-3213(81)90006-7.

[3] M. Dine, W. Fischler, and M. Srednicki, "Supersymmetric Technicolor", *Nucl. Phys. B* **189** (1981) 575, doi:10.1016/0550-3213(81)90582-4.

[4] S. Dimopoulos and H. Georgi, "Softly Broken Supersymmetry and SU(5)", *Nucl. Phys. B* **193** (1981) 150, doi:10.1016/0550-3213(81)90522-8.

[5] N. Sakai, "Naturalness in Supersymmetric Guts", *Z. Phys. C* **11** (1981) 153, doi:10.1007/BF01573998.

[6] R. K. Kaul and P. Majumdar, "Cancellation of quadratically divergent mass corrections in globally supersymmetric spontaneously broken gauge theories", *Nucl. Phys. B* **199** (1982) 36, doi:10.1016/0550-3213(82)90565-X.

[7] CMS Collaboration, "The CMS experiment at the CERN LHC", *J. Inst* **3** (2008) S08004, doi:10.1088/1748-0221/3/08/S08004.

[8] CMS Collaboration, "Search for direct top squark production in events with a single isolated lepton, jets and missing transverse energy at $\sqrt{s}$ = 8 TeV",. CMS-PAS-SUS-12-023.

[9] R. Barbieri and G. Giudice, "Upper Bounds on Supersymmetric Particle Masses", *Nucl. Phys. B* **306** (1988) 63, doi:10.1016/0550-3213(88)90171-X.

[10] B. de Carlos and J. Casas, "One-loop analysis of the electroweak breaking in supersymmetric models and the fine-tuning problem", *Phys. Lett. B* **309** (1993), no. 34, 320, doi:10.1016/0370-2693(93)90940-J.

[11] S. Dimopoulos and G. Giudice, "Naturalness constraints in supersymmetric theories with non-universal soft terms", *Phys. Lett. B* **357** (1995), no. 4, 573, doi:10.1016/0370-2693(95)00961-J.

[12] R. Barbieri, G. Dvali, and L. J. Hall, "Predictions from a U(2) flavour symmetry in supersymmetric theories", *Phys. Lett. B* **377** (1996), no. 13, 76, doi:10.1016/0370-2693(96)00318-8.

[13] M. Papucci, J. T. Ruderman, and A. Weiler, "Natural SUSY Endures", *JHEP* **1209** (2012) 035, doi:10.1007/JHEP09(2012)035, arXiv:1110.6926.

[14] M. W. Cahill-Rowley et al., "The Higgs Sector and Fine-Tuning in the pMSSM", *Phys. Rev. D* **86** (2012) 075015, doi:10.1103/PhysRevD.86.075015, arXiv:1206.5800.

[15] CMS Collaboration Collaboration, "Observation of a new boson at a mass of 125 GeV with the CMS experiment at the LHC", *Phys. Lett. B* **716** (2012) 30, doi:10.1016/j.physletb.2012.08.021, arXiv:1207.7235.

[16] ATLAS Collaboration Collaboration, "Observation of a new particle in the search for the Standard Model Higgs boson with the ATLAS detector at the LHC", *Phys. Lett. B* **716** (2012) 1, doi:10.1016/j.physletb.2012.08.020, arXiv:1207.7214.

[17] ATLAS Collaboration, "Search for a supersymmetric partner to the top quark in final states with jets and missing transverse momentum at $\sqrt{s} = 7$ TeV with the ATLAS detector", arXiv:1208.1447. Submitted to *Phys. Rev. Lett.*

[18] ATLAS Collaboration, "Search for direct top squark pair production in final states with one isolated lepton, jets, and missing transverse momentum in $\sqrt{s} = 7$ TeV pp collisions using 4.7 fb^{-1} of ATLAS data", arXiv:1208.2590. Submitted to *Phys. Rev. Lett.*

[19] ATLAS Collaboration, "Search for light scalar top quark pair production in final states with two leptons with the ATLAS detector in $\sqrt{s} = 7$ TeV proton-proton collisions", arXiv:1208.4305. Submitted to *Eur. Phys. J C*.

[20] ATLAS Collaboration, "Search for light top squark pair production in final states with leptons and b-jets with the ATLAS detector in $\sqrt{s} = 7$ TeV proton-proton collisions", arXiv:1209.2102. Submitted to *Phys. Lett. B*.

[21] ATLAS Collaboration, "Search for a heavy top-quark partner in final states with two leptons with the ATLAS detector at the LHC", arXiv:1209.4186. Submitted to *JHEP*.

[22] CDF Collaboration, "Search for the supersymmetric partner of the top quark in $p\bar{p}$ collisions at $\sqrt{s} = 1.96$ TeV", *Phys. Rev. D* **82** (2010) 092001, doi:10.1103/PhysRevD.82.092001, arXiv:1009.0266.

[23] D0 Collaboration, "Search for pair production of the scalar top quark in the electron+muon final state", *Phys. Lett. B* **696** (2011) 321, doi:10.1016/j.physletb.2010.12.052, arXiv:1009.5950.

[24] T. Sjöstrand, S. Mrenna, and P. Z. Skands, "PYTHIA 6.4 Physics and Manual", *JHEP* **05** (2006) 026, doi:10.1088/1126-6708/2006/05/026, arXiv:hep-ph/0603175.

[25] J. Alwall et al., "MadGraph 5 : Going Beyond", *JHEP* **1106** (2011) 128, doi:10.1007/JHEP06(2011)128, arXiv:1106.0522.

[26] S. Frixione and B. R. Webber, "Matching NLO QCD computations and parton shower simulations", *JHEP* **0206** (2002) 029, arXiv:hep-ph/0204244.

[27] S. Frixione, P. Nason, and B. R. Webber, "Matching NLO QCD and parton showers in heavy flavor production", *JHEP* **0308** (2003) 007, arXiv:hep-ph/0305252.

[28] S. Frixione, P. Nason, and C. Oleari, "Matching NLO QCD computations with parton shower simulations: the POWHEG method", *JHEP* **11** (2007) 070, doi:10.1088/1126-6708/2007/11/070, arXiv:0709.2092.

[29] P. M. Nadolsky et al., "Implications of CTEQ global analysis for collider observables", *Phys. Rev. D* **78** (2008) 013004, doi:10.1103/PhysRevD.78.013004, arXiv:0802.0007.

[30] N. Kidonakis, "Differential and total cross sections for top pair and single top production", doi:10.3204/DESY-PROC-2012-02/251, arXiv:1205.3453.

[31] J. M. Campbell and R. K. Ellis, "$t\bar{t}W^{+-}$ production and decay at NLO", *JHEP* **1207** (2012) 052, doi:10.1007/JHEP07(2012)052, arXiv:1204.5678.

[32] M. Garzelli et al., "t $\bar{t}$ W^{+-} and t $\bar{t}$ Z Hadroproduction at NLO accuracy in QCD with Parton Shower and Hadronization effects", *JHEP* **1211** (2012) 056, doi:10.1007/JHEP11(2012)056, arXiv:1208.2665.

[33] J. M. Campbell and R. Ellis, "MCFM for the Tevatron and the LHC", *Nucl.Phys.Proc.Suppl.* **205-206** (2010) 10–15, doi:10.1016/j.nuclphysbps.2010.08.011, arXiv:1007.3492.

[34] R. Gavin et al., "W Physics at the LHC with FEWZ 2.1", *Comput.Phys.Commun.* **184** (2013) 208–214, doi:10.1016/j.cpc.2012.09.005, arXiv:1201.5896.

[35] R. Frederix et al., "Four-lepton production at hadron colliders: aMC@NLO predictions with theoretical uncertainties", *JHEP* **1202** (2012) 099, doi:10.1007/JHEP02(2012)099, arXiv:1110.4738.

[36] M. Perelstein and A. Weiler, "Polarized Tops from Stop Decays at the LHC", *JHEP* **0903** (2009) 141, doi:10.1088/1126-6708/2009/03/141, arXiv:0811.1024.

[37] I. Low, "Polarized Charginos (and Tops) in Stop Decays", arXiv:1304.0491.

[38] M. Kramer et al., "Supersymmetry production cross sections in pp collisions at $\sqrt{s}$ = 7 TeV", arXiv:1206.2892.

[39] CMS Collaboration, "The fast simulation of the CMS detector at LHC", *J. Phys. Conf. Ser.* **331** (2011) 032049, doi:10.1088/1742-6596/331/3/032049.

[40] GEANT4 Collaboration, "GEANT4–a simulation toolkit", *Nucl. Instrum. Meth. A* **506** (2003) 250, doi:10.1016/S0168-9002(03)01368-8.

[41] CMS Collaboration, "Performance of muon identification in pp collisions at $\sqrt{s}$ = 7 TeV", CMS Physics Analysis Summary CMS-PAS-MUO-10-002, (2010).

[42] CMS Collaboration, "Electron Reconstruction and Identification at $\sqrt{s} = 7$ TeV", CMS Physics Analysis Summary CMS-PAS-EGM-10-004, (2010).

[43] CMS Collaboration, "Commissioning of the Particle-Flow Reconstruction in Minimum-Bias and Jet Events from pp Collisions at 7 TeV", CMS Physics Analysis Summary CMS-PAS-PFT-10-002, (2010).

[44] M. Cacciari, G. P. Salam, and G. Soyez, "The anti-k_t jet clustering algorithm", *JHEP* **04** (2008) 063, doi:10.1088/1126-6708/2008/04/063, arXiv:0802.1189.

[45] M. Cacciari and G. P. Salam, "Dispelling the N^3 myth for the k_t jet-finder", *Phys. Lett. B* **641** (2006) 57, doi:10.1016/j.physletb.2006.08.037.

[46] M. Cacciari, G. Salam, and G. Soyez, "FastJet user manual", 2011, arXiv:1111.6097.

[47] M. Cacciari and G. P. Salam, "Pileup subtraction using jet areas", *Phys. Lett. B* **659** (2008) 119, doi:10.1016/j.physletb.2007.09.077.

[48] CMS Collaboration Collaboration, "Identification of b-quark jets with the CMS experiment", *JINST* **8** (2013) P04013, doi:10.1088/1748-0221/8/04/P04013, arXiv:1211.4462.

[49] Y. Bai et al., "Stop the Top Background of the Stop Search", *JHEP* **1207** (2012) 110, doi:10.1007/JHEP07(2012)110, arXiv:1203.4813.

[50] Particle Data Group Collaboration, "Review of Particle Physics (RPP)", *Phys.Rev.* **D86** (2012) 010001, doi:10.1103/PhysRevD.86.010001.

[51] A. L. Read, "Presentation of search results: the CL_S technique", *J. Phys. G* **28** (2002) 2693, doi:10.1088/0954-3899/28/10/313.

[52] T. Junk, "Confidence level computation for combining searches with small statistics", *Nucl. Instrum. Meth. A* **434** (1999) 435, doi:10.1016/S0168-9002(99)00498-2, arXiv:hep-ex/9902006.

[53] ATLAS and CMS Collaborations, LHC Higgs Combination Group, "Procedure for the LHC Higgs boson search combination in Summer 2011", ATL-PHYS-PUB/CMS NOTE 2011-11, 2011/005, (2011).

A Further information about systematic uncertainties

The systematic uncertainties for the $\tilde{t} \to t\tilde{\chi}_1^0$ cut-based, $\tilde{t} \to b\tilde{\chi}_1^+$ cut-based and BDT analyses are shown in Tables. 7, 8 and 9 respectively.

Sample	$E_T^{miss} > 150$ GeV	$E_T^{miss} > 200$ GeV	$E_T^{miss} > 250$ GeV	$E_T^{miss} > 300$ GeV
Low ΔM Selection				
M_T peak data and MC (stat)	1.4	2.4	4.0	6.3
$t\bar{t} \to \ell^+\ell^-$ N_{jets} modeling	1.6	1.5	1.6	1.5
$t\bar{t} \to \ell^+\ell^-$ (CR-ℓt and CR-2ℓ tests)	5.2	7.6	13.1	19.6
2nd lepton veto	1.3	1.2	1.3	1.2
$t\bar{t} \to \ell^+\ell^-$ (stat)	1.9	3.2	5.2	8.0
W+jets cross section	1.1	1.1	1.8	2.2
W+jets (stat)	2.1	3.2	4.1	5.6
W+jets SF uncertainty	9.4	9.0	7.5	7.0
1-ℓ Top (stat)	0.6	0.9	1.1	1.5
1-ℓ Top tail-to-peak ratio	16.0	20.7	18.3	18.5
rare cross sections	2.0	2.6	3.8	5.9
Total	19.8	24.6	25.5	30.9
High ΔM Selection				
M_T peak data and MC (stat)	3.9	4.8	6.0	8.5
$t\bar{t} \to \ell^+\ell^-$ N_{jets} modeling	0.8	0.9	1.0	0.9
$t\bar{t} \to \ell^+\ell^-$ (CR-ℓt and CR-2ℓ tests)	4.1	6.1	11.7	14.9
2nd lepton veto	0.7	0.7	0.8	0.7
$t\bar{t} \to \ell^+\ell^-$ (stat)	4.2	5.9	8.4	10.2
W+jets cross section	0.6	0.5	1.3	1.8
W+jets (stat)	3.8	4.7	5.7	7.7
W+jets SF uncertainty	11.7	10.3	8.8	8.8
1-ℓ Top (stat)	1.8	1.9	2.1	3.4
1-ℓ Top tail-to-peak ratio	17.1	21.3	20.9	17.3
rare cross sections	6.1	6.9	7.8	9.2
Total	23.1	27.0	29.3	30.6

Table 7: The bottom row of this table shows the relative uncertainty (in percent) on the total background predictions for the $\tilde{t} \to t\tilde{\chi}_1^0$ cut-based signal regions. The breakdown of this total uncertainty in its individual components is also shown.

Sample	$E_{\mathrm{T}}^{\mathrm{miss}} > 100$ GeV	$E_{\mathrm{T}}^{\mathrm{miss}} > 150$ GeV	$E_{\mathrm{T}}^{\mathrm{miss}} > 200$ GeV	$E_{\mathrm{T}}^{\mathrm{miss}} > 250$ GeV
Low ΔM Selection				
M_{T} peak data and MC (stat)	0.7	1.3	2.2	3.5
$\mathrm{t\bar{t}} \to \ell^+\ell^-$ $\mathrm{N_{jets}}$ modeling	1.6	1.9	1.9	1.9
$\mathrm{t\bar{t}} \to \ell^+\ell^-$ (CR-ℓt and CR-2ℓ tests)	2.6	3.2	6.4	12.4
2nd lepton veto	1.3	1.5	1.5	1.5
$\mathrm{t\bar{t}} \to \ell^+\ell^-$ (stat)	0.7	1.4	2.4	3.9
W+jets cross section	1.5	2.0	2.5	3.2
W+jets (stat)	0.8	1.1	1.6	2.2
W+jets SF uncertainty	9.9	6.8	5.7	5.4
1-ℓ Top (stat)	0.3	0.4	0.5	0.7
1-ℓ Top tail-to-peak ratio	5.9	11.0	11.7	12.1
rare cross sections	1.1	1.7	2.6	3.7
Total	12.2	14.0	15.6	19.7
High ΔM Selection				
M_{T} peak data and MC (stat)	2.9	3.3	4.3	5.5
$\mathrm{t\bar{t}} \to \ell^+\ell^-$ $\mathrm{N_{jets}}$ modeling	1.0	0.9	1.1	0.9
$\mathrm{t\bar{t}} \to \ell^+\ell^-$ (CR-ℓt and CR-2ℓ tests)	4.8	6.3	10.6	13.4
2nd lepton veto	0.9	0.8	0.9	0.8
$\mathrm{t\bar{t}} \to \ell^+\ell^-$ (stat)	2.6	3.9	5.6	7.1
W+jets cross section	2.3	1.5	1.6	1.5
W+jets (stat)	1.8	2.5	3.2	4.3
W+jets SF uncertainty	11.5	10.2	8.4	8.3
1-ℓ Top (stat)	1.3	1.5	1.5	1.6
1-ℓ Top tail-to-peak ratio	5.2	12.5	15.3	16.6
rare cross sections	4.1	7.0	8.7	10.2
Total	15.0	19.7	23.7	27.1

Table 8: The bottom row of this table shows the relative uncertainty (in percent) on the total background predictions for the $\tilde{\mathrm{t}} \to \mathrm{b}\widetilde{\chi}_1^+$ cut-based signal regions. The breakdown of this total uncertainty in its individual components is also shown.

$\tilde{t} \to b\tilde{\chi}_1^+$ $x = 0.75$				
Sample	BDT1	BDT2	BDT3	BDT4
M_T peak data and MC (stat)	3.5	5.3	7.8	1.2
$t\bar{t} \to \ell^+\ell^-$ N_{jets} modeling	1.8	1.2	1.1	1.6
$t\bar{t} \to \ell^+\ell^-$ (CR-ℓt and CR-2ℓ tests)	6.0	8.2	11.3	3.6
2nd lepton veto	1.7	1.1	1.0	1.4
$t\bar{t} \to \ell^+\ell^-$ (stat)	4.3	5.9	9.6	1.4
W+jets cross section	2.7	2.3	2.7	1.4
W+jets (stat)	4.5	5.3	6.4	2.4
W+jets SF uncertainty	6.9	7.7	7.0	9.9
1-ℓ Top (stat)	1.2	1.2	1.2	0.6
1-ℓ Top tail-to-peak ratio	11.3	19.5	17.6	10.7
rare cross sections	1.9	6.2	8.9	1.1
Total	16.8	25.4	27.8	15.5

$\tilde{t} \to b\tilde{\chi}_1^+$ $x = 0.5$				
Sample	BDT1	BDT2 Loose	BDT2 Tight	BDT3
M_T peak data and MC (stat)	3.0	3.3	6.0	5.8
$t\bar{t} \to \ell^+\ell^-$ N_{jets} modeling	1.6	1.3	1.0	1.1
$t\bar{t} \to \ell^+\ell^-$ (CR-ℓt and CR-2ℓ tests)	5.2	6.4	17.2	11.1
2nd lepton veto	1.4	1.2	1.0	1.0
$t\bar{t} \to \ell^+\ell^-$ (stat)	3.5	4.0	6.6	6.2
W+jets cross section	2.5	2.6	1.4	3.3
W+jets (stat)	2.3	2.2	4.1	3.4
W+jets SF uncertainty	8.0	8.0	8.1	7.3
1-ℓ Top (stat)	1.0	1.2	1.5	1.6
1-ℓ Top tail-to-peak ratio	10.3	11.5	18.4	11.7
rare cross sections	3.3	6.8	8.7	9.4
Total	15.7	18.0	29.7	22.3

$\tilde{t} \to b\tilde{\chi}_1^+$ $x = 0.25$		
Sample	BDT2	BDT3
M_T peak data and MC (stat)	9.0	10.6
$t\bar{t} \to \ell^+\ell^-$ N_{jets} modeling	0.7	0.8
$t\bar{t} \to \ell^+\ell^-$ (CR-ℓt and CR-2ℓ tests)	11.4	19.1
2nd lepton veto	0.6	0.8
$t\bar{t} \to \ell^+\ell^-$ (stat)	6.5	11.8
W+jets cross section	1.0	1.5
W+jets (stat)	5.3	6.7
W+jets SF uncertainty	11.3	9.5
1-ℓ Top (stat)	3.2	4.2
1-ℓ Top tail-to-peak ratio	12.6	13.2
rare cross sections	6.2	9.6
Total	24.9	32.3

Table 9: The bottom row of this table shows the relative uncertainty (in percent) on the total background predictions for the $\tilde{t} \to b\tilde{\chi}_1^+$ BDT signal regions. The breakdown of this total uncertainty in its individual components is also shown.

B Monte Carlo modeling of initial-state radiation

The experimental acceptance for signal events depends on initial-state radiation (ISR). As the simulation is not necessarily expected to model ISR well, we validate the simulation by comparing MADGRAPH MC predictions with data. The predicted p_T spectrum of the system recoiling against the ISR jets is compared to data in Z+jets, $t\bar{t}$, and WZ final states. These processes can be measured with sufficient statistical precision in data and cover a variety of masses and initial states.

Z+jets events are selected by requiring exactly two opposite-sign, same-flavor leptons (ee or $\mu\mu$) with an invariant mass between 81 and 101 GeV. Events for this selection as well as $t\bar{t}$ and WZ events are selected with dilepton triggers. Events with at least one b-tagged jet or with additional lepton candidates are vetoed to remove contributions from $t\bar{t}$ and diboson (WZ/ZZ) production, respectively. In Z+jets events, the Z boson is expected to be balanced in transverse momentum with the ISR jet system. The p_T of the Z boson is thus computed in two ways: as the p_T of the dilepton system, and, for events with at least one reconstructed jet, as the p_T of the vector sum of the reconstructed jets, termed the "jet system" p_T. The predicted MC spectrum for each quantity is compared with data, as shown in Fig. 13. The MC prediction is normalized to the total data yield so that the shapes can be readily compared. The correction applied to the MC is 4%, consistent within the uncertainty on the integrated luminosity. Good agreement is observed at lower p_T, while at higher p_T the MC predictions lie above the data. The simulation is about 10% too high for $p_T = 150$ GeV and 20% for $p_T = 250$ GeV. Both quantities show the same trend, validating the jet recoil method of measuring this quantity. The dilepton p_T and jet system p_T were also checked for events with exactly one, two, or three jets, as well as at least four jets, and in each case the results were consistent with the inclusive results shown in Fig. 13. The impact of the jet energy scale uncertainty, which only affects the jet system p_T, was found to be much smaller than the observed discrepancies.

Dilepton $t\bar{t}$ events are selected by requiring an opposite-sign eμ pair and exactly two b-tagged jets. Events containing a third lepton candidate are vetoed. These requirements select dilepton $t\bar{t}$ events with high purity (about 97% in simulation) and unambiguously identify all the visible $t\bar{t}$ decay products. Because of the presence of neutrinos in the $t\bar{t}$ decays, the p_T of the $t\bar{t}$ cannot be directly measured but can be inferred from the ISR jet recoil system. Additional jets beyond the two b-tagged jets in these events are thus considered to be ISR jets for the purposes of this study, and the "jet system" is formed by the vector sum of ISR jets. The p_T of the jet system defined this way was found in simulation to reproduce well the p_T of the generated $t\bar{t}$ system. The predicted jet system p_T spectrum is compared with data in Fig. 14. Good agreement is observed at lower p_T. At higher p_T, the simulation is consistent with the data to within the uncertainties, but it also exhibits a trend to overpredict the data, as in the case of Z+jets events. The jet system p_T was also checked for events with exactly one, two, or three jets, as well as at least four jets, and in each case the results were consistent with the inclusive results shown in Fig. 14. Again, the effect of the jet energy scale uncertainty was examined and was found to be small.

Finally, WZ $\to \ell\nu\ell\ell$ events are selected by requiring exactly three leptons, with two opposite-sign same-flavor leptons (ee or $\mu\mu$) consistent with the Z boson mass and a third lepton (e or μ) with $M_T > 50$ GeV. Events with at least one b-tagged jet are vetoed. The expected purity of this selection from simulation is about 83%, with about 7% of events coming from ZZ production. As with $t\bar{t}$ events, the neutrino in the final state prevents a direct measurement of the WZ system p_T, but the jet recoil system can be used and is defined in the same way as for the Z+jets sample. In data, this selection yields on the order of 1000 events, so the statistical uncertainty

at high values of jet system p_T is large. As for the $t\bar{t}$ MC events, the WZ simulation is found to be consistent with the data to within the uncertainties, but also shows a trend to overpredict the data at large p_T that is consistent with the level observed for the Z+jets events

Given the MC overprediction observed in the high-statistics Z+jets final state, and the consistency of the other final states with this result, weights are derived to correct the MC prediction as a function of the p_T of the system recoiling against ISR jets. These weights are applied to the MADGRAPH signal samples used in this analysis, and the full values of the corrections are taken as a systematic uncertainty. This procedure is considered to be conservative as it lowers the predicted MC acceptance for a given signal. The values of the weights range from 0–20% depending on the p_T of the system recoiling against ISR jets. The blue bands shown on the ratio plots in Figs. 13–14 are centered on the weighted MC prediction, with the width of the band showing the associated uncertainty.

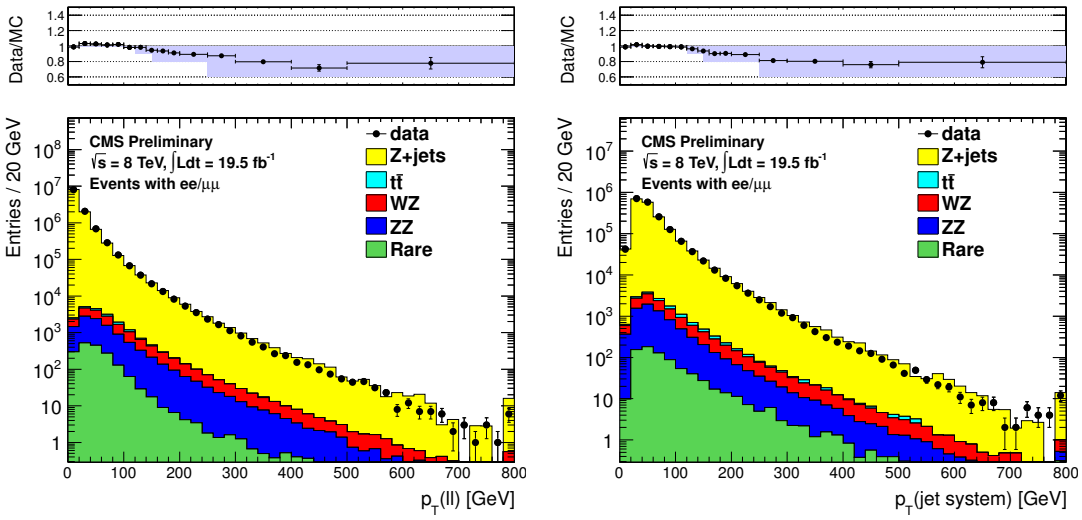

Figure 13: Comparison of data to MC predictions for the dilepton p_T (left) and jet recoil system p_T (right) in Z+jets events. The MC prediction is normalized to the total data yield to compare the shapes of the distributions. The ratio of data/MC is shown at the top of the figure. The light blue band shows the weights derived for simulation and the variation to assess systematic uncertainties.

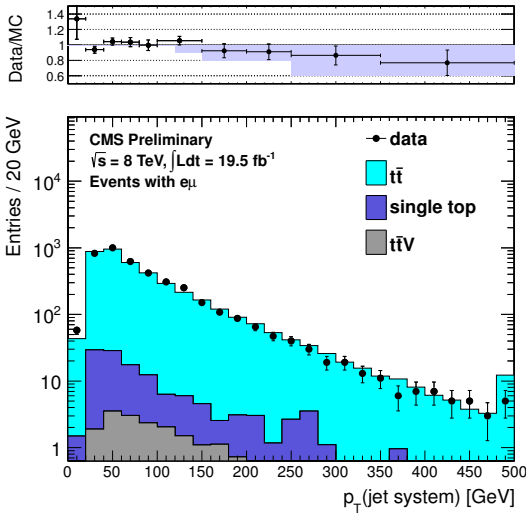

Figure 14: Comparison of data to MC prediction for the jet recoil system p_{T} in $\mathrm{t\bar{t}}$ events. The MC prediction is normalized to the total data yield to compare the shapes of the distributions. The ratio of data/MC is shown at the top of the figure. The light blue band shows the weights derived for MC and the variation to assess systematic uncertainties.

C Additional M_T and BDT Output Distributions

In this section, additional M_T and BDT output distributions are presented for the $\tilde{t} \to t\tilde{\chi}_1^0$ (Figs. 15-16) and $\tilde{t} \to b\tilde{\chi}_1^+$ (Figs. 17-20) BDT signal regions.

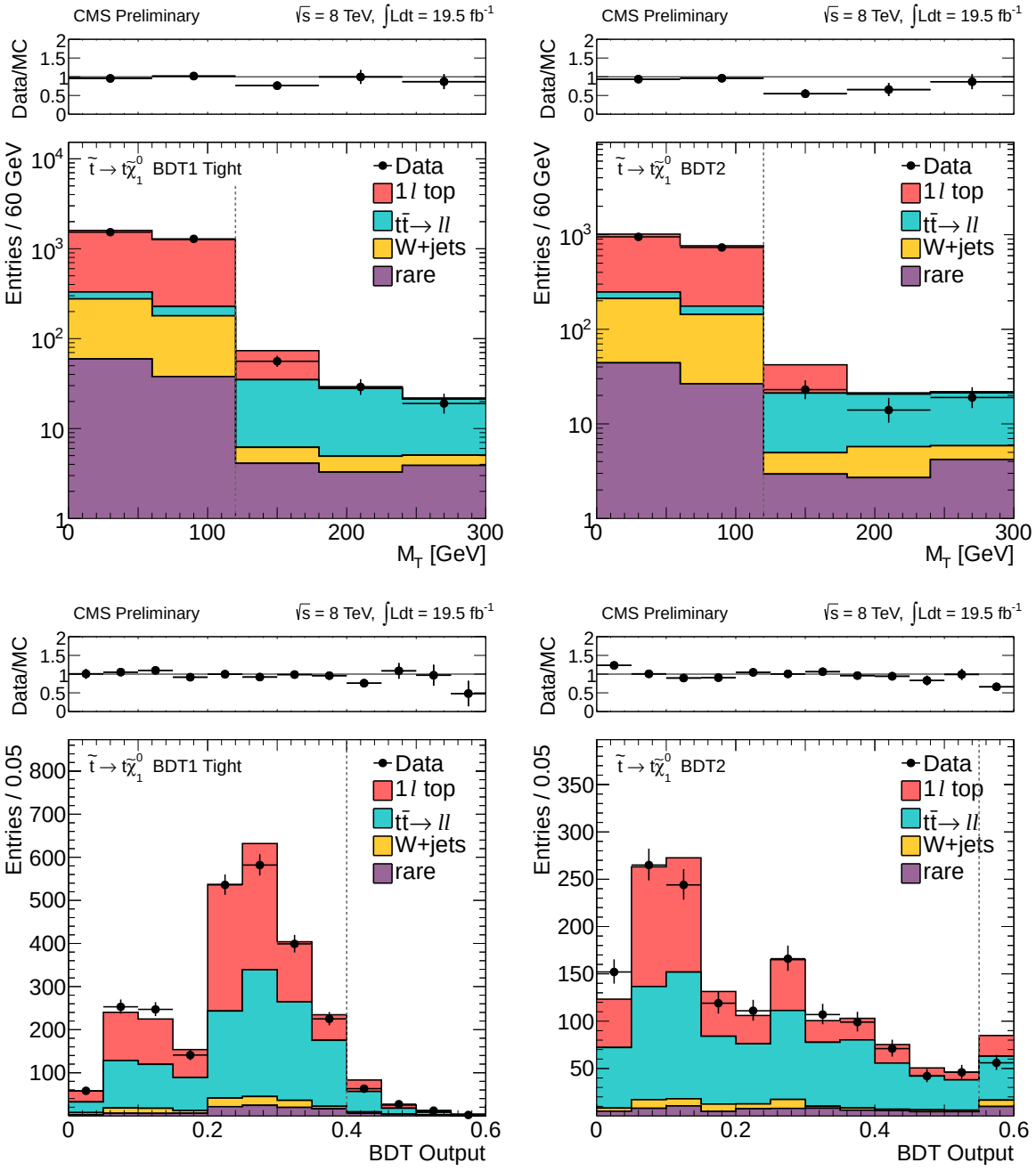

Figure 15: Comparison of the M_T (top) and BDT output (bottom) distributions in data vs. MC for events satisfying the BDT1 tight (left) and BDT2 (right) $\tilde{t} \to t\tilde{\chi}_1^0$ BDT signal region requirements. In the M_T plots, the BDT output signal region requirement is imposed; in the BDT plots, the $M_T > 120$ GeV requirement is imposed. The vertical dashed line indicates the corresponding signal region requirement.

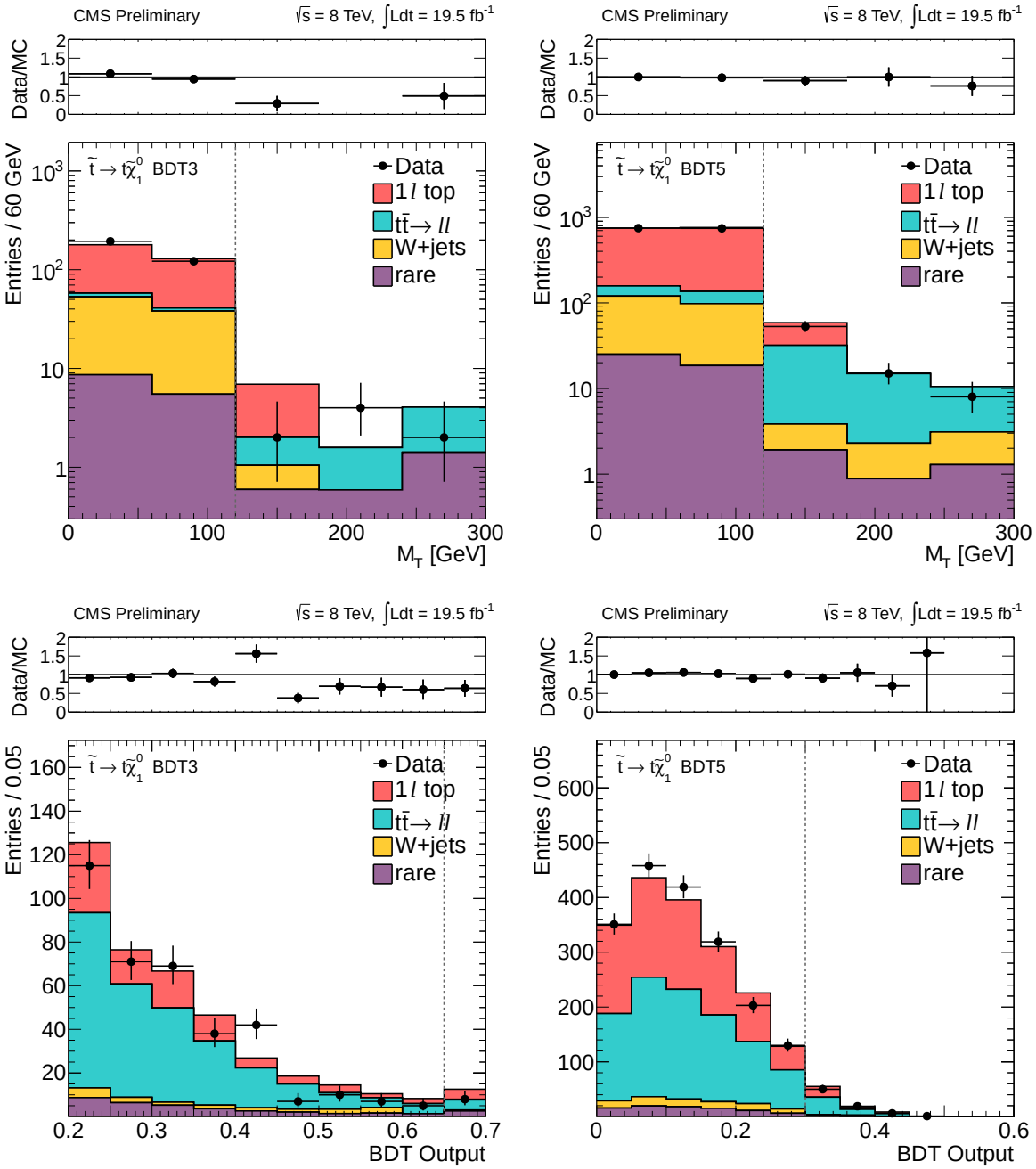

Figure 16: Comparison of the M_{T} (top) and BDT output (bottom) distributions in data vs. MC for events satisfying the BDT3 (left) and BDT5 (right) $\tilde{\mathrm{t}} \to \mathrm{t}\tilde{\chi}_1^0$ BDT signal region requirements. In the M_{T} plots, the BDT output signal region requirement is imposed; in the BDT plots, the $M_{\mathrm{T}} > 120$ GeV requirement is imposed. The vertical dashed line indicates the corresponding signal region requirement.

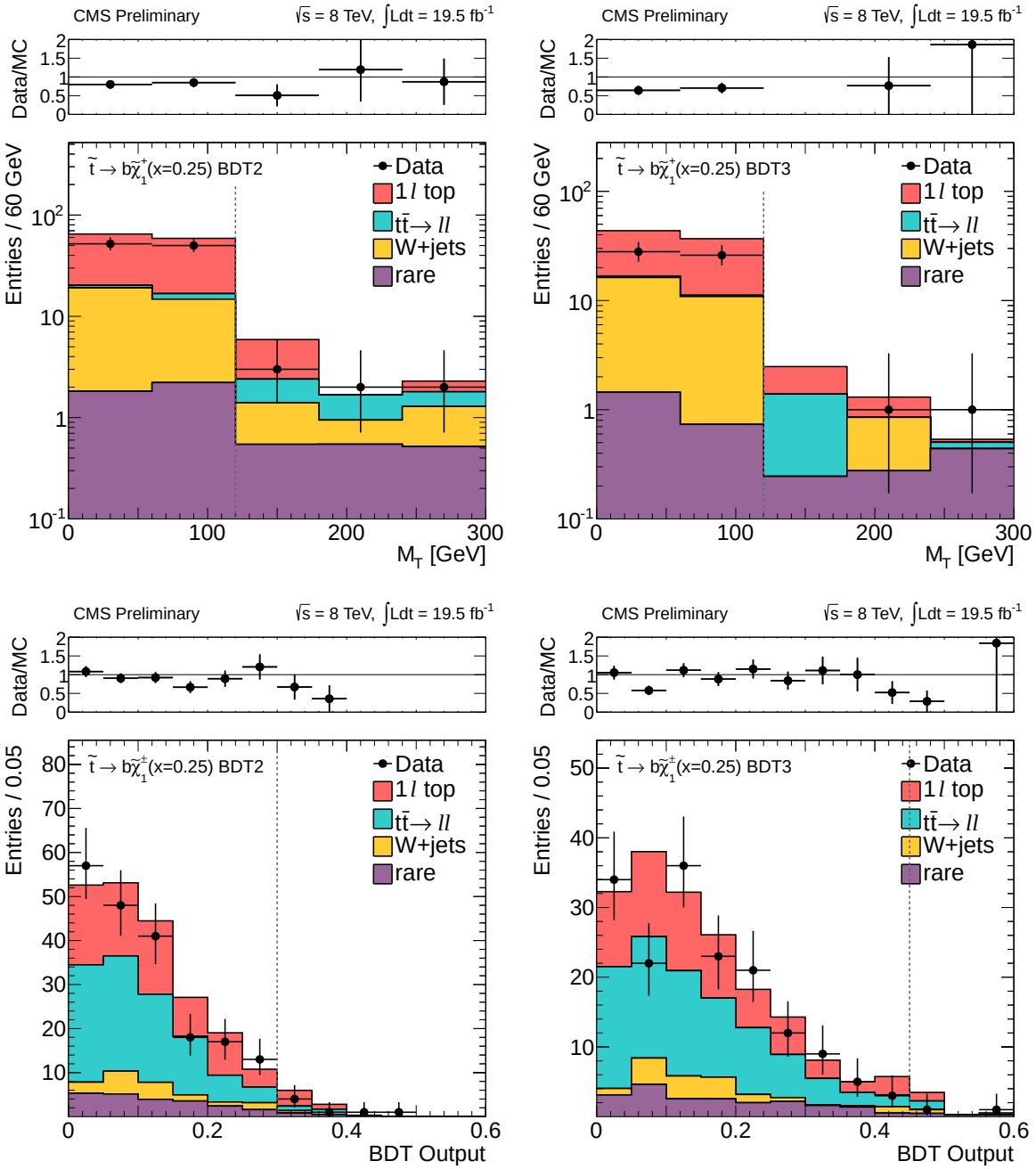

Figure 17: Comparison of the M_T (top) and BDT output (bottom) distributions in data vs. MC for events satisfying the BDT2 (left) and BDT3 (right) $\tilde{t} \to b\tilde{\chi}_1^+$ $x = 0.25$ BDT signal region requirements. In the M_T plots, the BDT output signal region requirement is imposed; in the BDT plots, the $M_T > 120$ GeV requirement is imposed. The vertical dashed line indicates the corresponding signal region requirement.

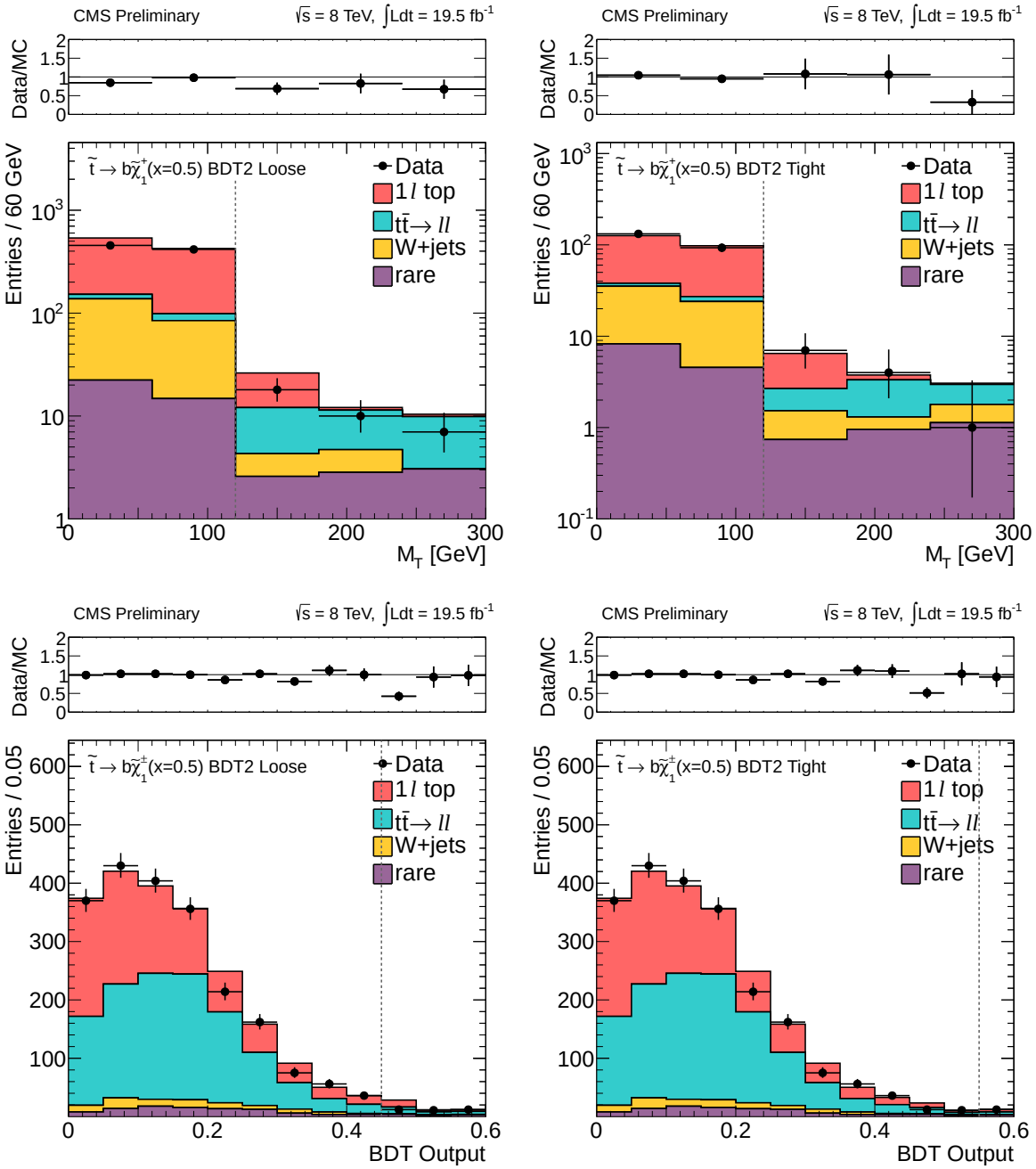

Figure 18: Comparison of the M_{T} (top) and BDT output (bottom) distributions in data vs. MC for events satisfying the BDT2 loose (left) and BDT2 tight (right) $\tilde{\mathrm{t}} \to \mathrm{b}\tilde{\chi}_1^+$ $x = 0.5$ BDT signal region requirements. In the M_{T} plots, the BDT output signal region requirement is imposed; in the BDT plots, the $M_{\mathrm{T}} > 120$ GeV requirement is imposed. The vertical dashed line indicates the corresponding signal region requirement.

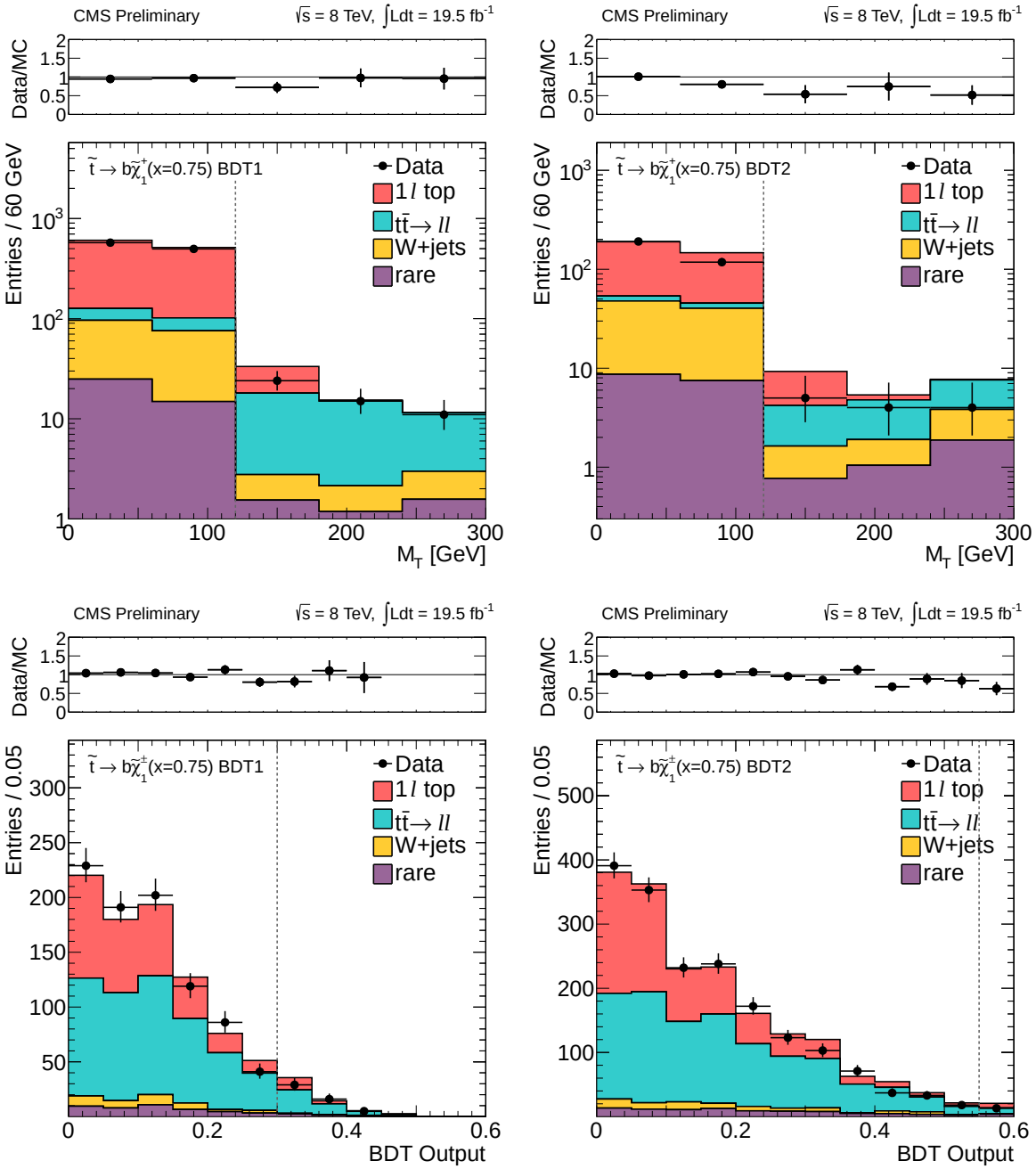

Figure 19: Comparison of the M_T (top) and BDT output (bottom) distributions in data vs. MC for events satisfying the BDT1 (left) and BDT2 (right) $\tilde{t} \to b\tilde{\chi}_1^+$ $x = 0.75$ BDT signal region requirements. In the M_T plots, the BDT output signal region requirement is imposed; in the BDT plots, the $M_T > 120$ GeV requirement is imposed. The vertical dashed line indicates the corresponding signal region requirement.

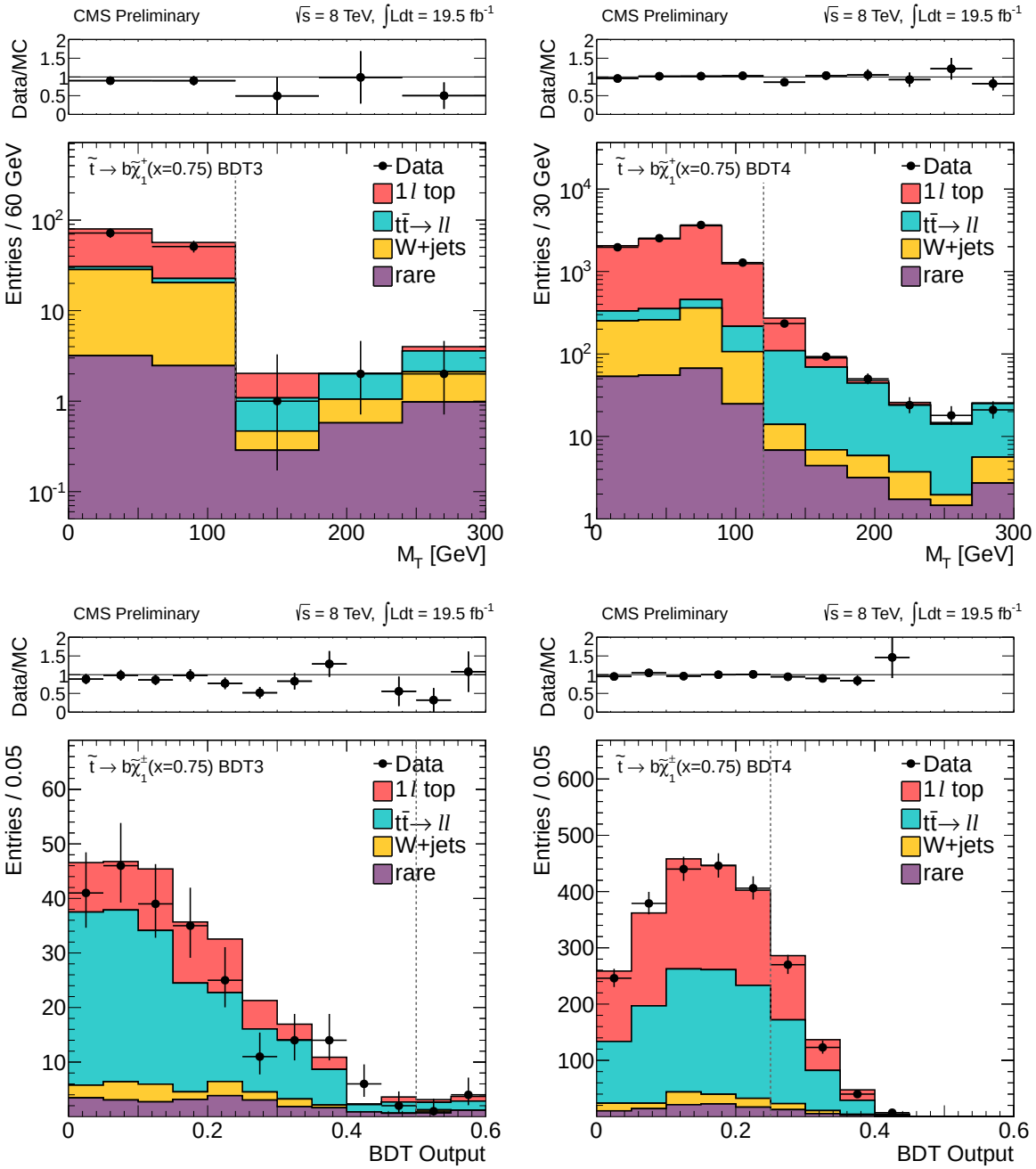

Figure 20: Comparison of the M_{T} (top) and BDT output (bottom) distributions in data vs. MC for events satisfying the BDT3 (left) and BDT4 (right) $\tilde{\mathrm{t}} \to \mathrm{b}\tilde{\chi}_1^+$ $x = 0.75$ BDT signal region requirements. In the M_{T} plots, the BDT output signal region requirement is imposed; in the BDT plots, the $M_{\mathrm{T}} > 120$ GeV requirement is imposed. The vertical dashed line indicates the corresponding signal region requirement.

D Further information about model interpretations

The interpretations for the $\tilde{t} \to t\tilde{\chi}_1^0$ and $\tilde{t} \to b\tilde{\chi}_1^+$ scenarios, using the cut-based analysis, are presented in Fig. 21. The most sensitive signal regions for the cut-based analysis and BDT analyses are presented in Figs. 22 and 23. The variations in the $\tilde{t} \to b\tilde{\chi}_1^+$ $x = 0.25$ and $x = 0.75$ limits due to assumptions about particle polarizations are presented in Fig. 24.

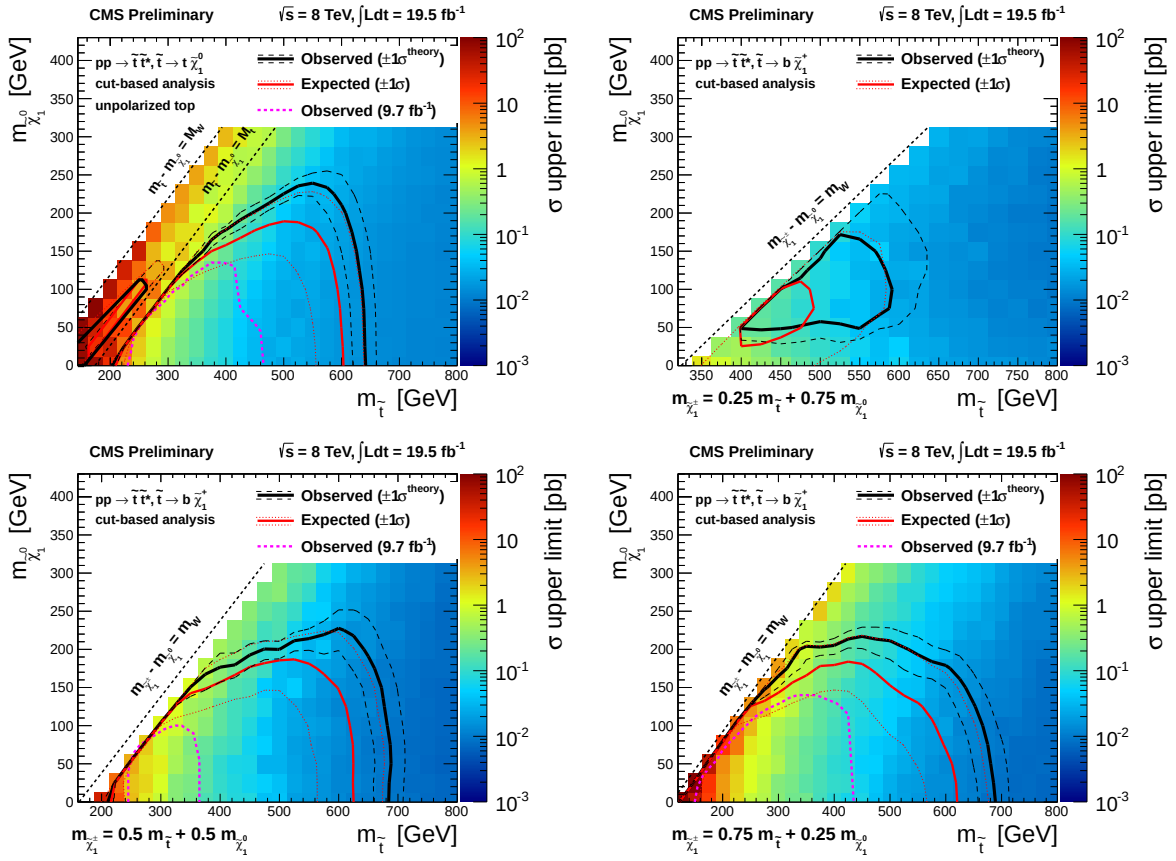

Figure 21: Interpretations based on the results of the cut-based analysis, for the (top left) $\tilde{t} \to t\tilde{\chi}_1^0$ model, and the $\tilde{t} \to b\tilde{\chi}_1^+$ model with chargino mass parameter (top right) $x = 0.25$, (bottom left) $x = 0.5$, and (bottom right) $x = 0.75$. The color scale indicates the observed cross section upper limit. The observed (solid black), median expected (solid red), and $\pm 1\sigma$ expected (dotted red) exclusion contours are indicated. The variations in the excluded region due to $\pm 1\sigma$ variations of the theoretical predictions for the signal cross sections are also indicated.

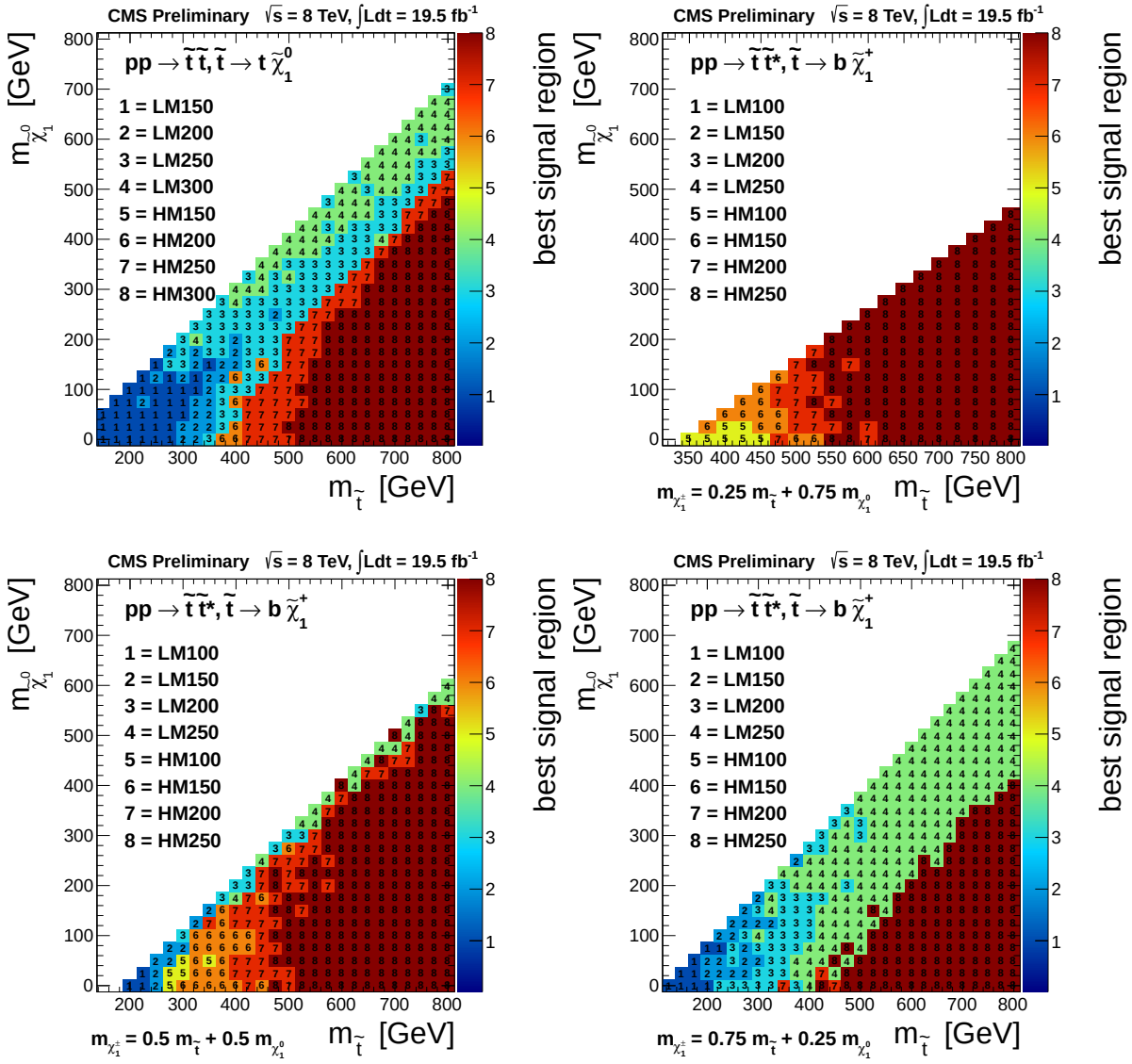

Figure 22: The most sensitive signal region in the $m_{\tilde{\chi}_1^0}$ vs. $m_{\tilde{t}}$ parameter space in the cut-based analysis, for the (top left) $\tilde{t} \to t\tilde{\chi}_1^0$ model, and the $\tilde{t} \to b\tilde{\chi}_1^+$ model with chargino mass parameter (top right) $x = 0.25$, (bottom left) $x = 0.5$, and (bottom right) $x = 0.75$. LM and HM refer to low ΔM and high ΔM, respectively, and the number indicates the $E_{\mathrm{T}}^{\mathrm{miss}}$ requirement.

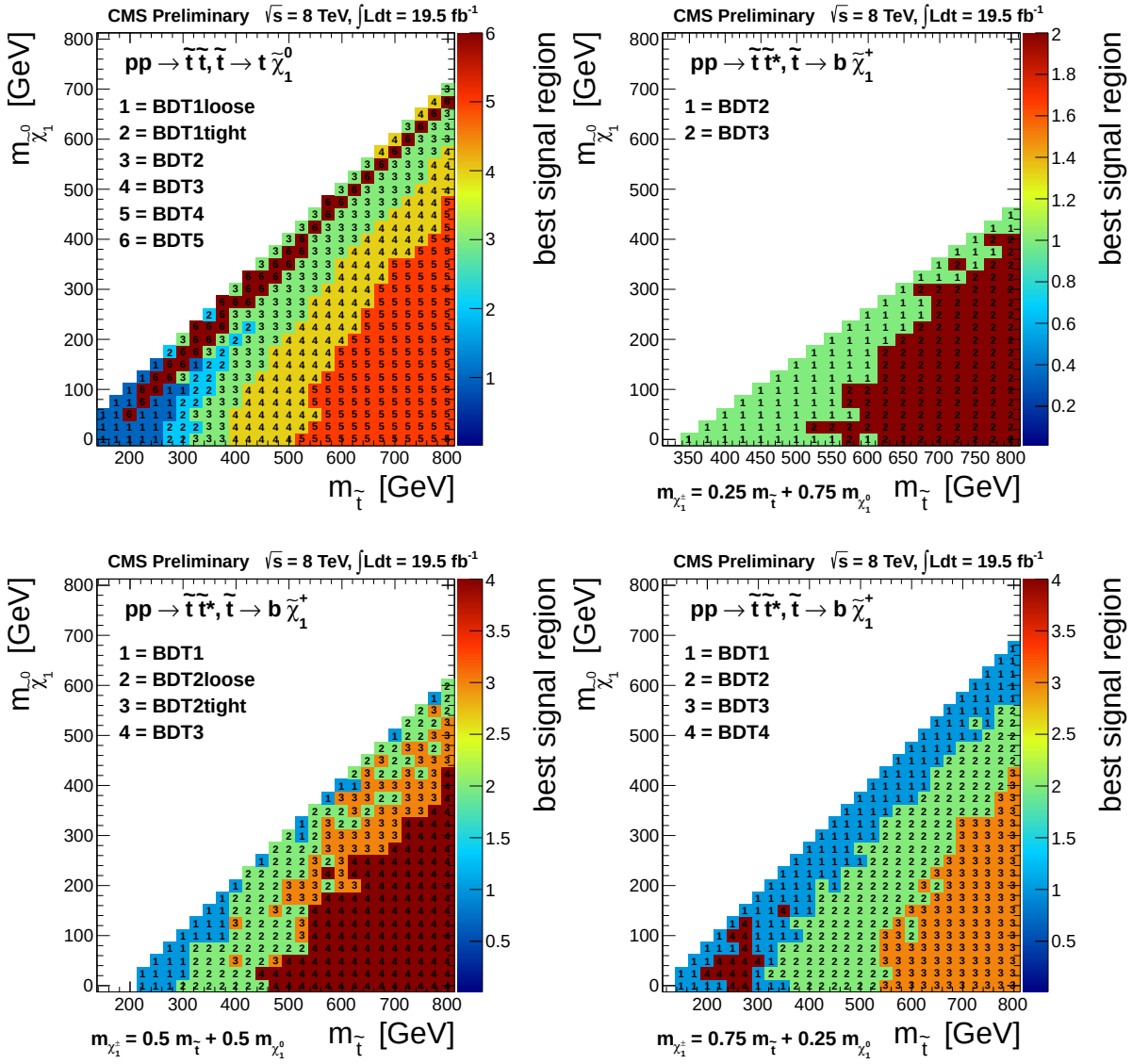

Figure 23: The most sensitive signal region in the $m_{\tilde{\chi}_1^0}$ vs. $m_{\tilde{t}}$ parameter space in the BDT analysis, for the (top left) $\tilde{t} \to t\tilde{\chi}_1^0$ model, and the $\tilde{t} \to b\tilde{\chi}_1^+$ model with chargino mass parameter (top right) $x = 0.25$, (bottom left) $x = 0.5$, and (bottom right) $x = 0.75$. The number indicates the BDT training region.

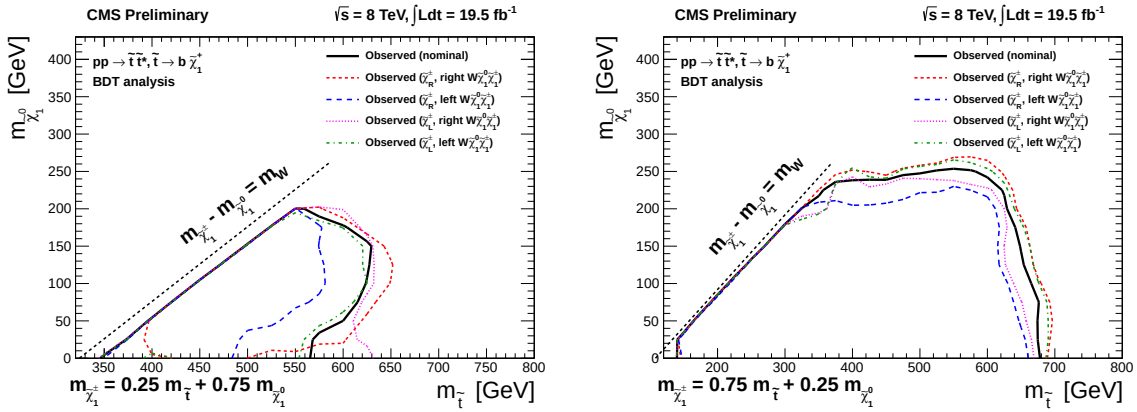

Figure 24: The observed excluded regions for the $\tilde{t} \to b\widetilde{\chi}_1^+$ model with $x = 0.25$ (left) and $x = 0.75$ (right) for the nominal scenario in our signal MC, right-handed vs. left-handed charginos ($\tilde{\chi}_R^{\pm}$ and $\tilde{\chi}_R^{\pm}$, respectively), and right-handed vs. left-handed $W\widetilde{\chi}_1^0\widetilde{\chi}_1^{\pm}$ couplings